공학박사학위논문

Highly Efficient Synthesis of Semiconductor Nanoparticles Using Spark Discharge

스파크 방전법을 이용한 반도체 나노입자의 고효율 합성법

2018 년 2 월

서울대학교 대학원

기계항공공학부

이 동 준

Highly Efficient Synthesis of Semiconductor Nanoparticles Using Spark Discharge

스파크 방전법을 이용한 반도체 나노입자의 고효율 합성법

지도교수 최 만 수

이 논문을 공학박사 학위논문으로 제출함

2017 년 11 월

서울대학교 대학원

기계항공공학부

이 동 준

이동준의 공학박사 학위논문을 인준함

2017 년 12 월

위 원 장 : 고 승 환 (인)

부위원장 : 최 만 수 (인)

위 원 : 이 윤 성 (인)

위 원 : 성 영 은 (인)

위 원 : 김 형 천 (인)

Highly Efficient Synthesis of Semiconductor Nanoparticles Using Spark Discharge

Dongjoon Lee
Department of Mechanical and Aerospace Engineering
The Graduate School
Seoul National University

Abstract

Nanoparticles have been widely studied and used in various application due to their novel optical and electrical properties. Among various nanoparticles, Semiconductor nanocrystals, so-called quantum dots, have been greatly studied and applied in various application such as photovoltaics, lasers, and LEDs since they have unique property called quantum confinement effect, which varies the energy gap according to their size. Synthesizing methods of quantum dots have been significant topic of the research field of nanotechnology. Up to now, those semiconductor nanocrystals usually synthesized using colloidal methods, which have disadvantages such as hazardous precursor, impurities, and byproduct.

Many of aerosol based gas phase synthesis have been are considered as clean and efficient methods for producing functional nanomaterials, which could not fully satisfied with existing colloidal methods. Among those various methods, spark discharge generation method has been spotlighted for producing charged aerosols with simple and efficient setup. Moreover, nanoparticles generated through spark discharge is proper for sub-10 nm

particles. With these motivation, in this thesis, we develop the synthesizing method for semiconductor nanocrystals using spark discharge and improve the particle generation efficiency by enhancing durability and production capacity.

To synthesize semiconductor nanocrystals, we introduced hydrogen gas to the spark discharge system. By injecting hydrogen gas as carrier gas, reducing environment was created which effectively removed oxide particles. Moreover, dissociated hydrogen gas by high energy of spark discharge penetrated in the nanoparticles and aid in crystallization process. As a result, hydrogen passivated silicon nanoparticles with high purity and crystallinity were successfully synthesized through this method.

In addition, beyond group Ⅳ-semiconductor, gallium arsenide nanocrystals which are Ⅲ-Ⅴ semiconductor were synthesized with similar method. Since the hydrogen relaxation process was more complex and required certain energy, serial thermal sintering processes were additionally performed for crystallization process and defect curing. Highly crystalline and ideally stoichiometric GaAs nanocrystals were synthesized and quantum confinement effects were identified by measuring photoluminescence in visible light area.

In order to industrial use of these generated nanoparticles, we improved the long-time consistency of particle generation. A newly designed wire-in-hole type spark discharger was able to generate un-agglomerated nanoparticles with a constant size distribution over a long time, compared to the conventional spark dischargers which are rod-to-rod spark discharger and pin-to-plate spark discharger. The wire-in-hole spark discharger effectively suppressed changes of the electrode morphology and gap distance, which resulted in the minimal variation of the breakdown voltage and spark frequency.

Lastly, for mass production of nanoparticles, we presented the wire-to-plate

electrode configuration for maintaining stable state of spark discharge in the high-frequency region. Compared to the conventional generators, this novel generator have much higher electric field due to the asymmetric geometry of electrodes and much faster velocity in the particle generation zone, which effectively dissipated the residual plasma of post discharge. By using wire-to-plate spark discharge, the maximum stable spark frequency of 17.9 kHz was achieved and mass production rate of the nanoparticles was increased proportionally to the spark frequency.

Keywords: Spark discharge; Quantum dots; Hydrogen assisted spark discharge; Long-time consistency; high-frequency spark discharge

Student Number: 2011-22892

Contents

Nomenclature

C_{ext}	External capacitance
d_g	Geometric mean diameter
E_{spark}	Energy dissipated during spark discharge
R	Charging resistance
$V_{discharge}$	Discharge voltage between electrodes
$V_{electrode}$	Potential applied to electrode
V_{input}	Applied setting potential from HV power supply
σ_g	Geometric standard deviation

List of Figures

Chapter 1.

Introduction

1.1. Background of Research

Nanoparticles have consistently received great attention from researchers and been expected for having their distinguished unique properties from bulk materials (Karch et al., 1987; Kruis et al., 1998; Siegel, 1993). Novel optical, electronical, and electrochemical properties of nanoparticles led to the diverse utilization in various field of modern technology such as biosensors, photovoltaics and catalysts (Atwater & Polman, 2010; Daniel & Astruc, 2004; Haes & Van Duyne, 2002).

In those various kinds of nanoparticles, especially semiconductor nanocrystals, so-called quantum dots, have been vigorously studied for their quantum confinement effect which is change of energy bandgap according to their diameter (Moras et al., 1996). This allows tuning of emission wavelength of the nanoparticles by controlling their size, and applied to the various optical and electronical devices such as light emitting diodes, field effect transistors and photovoltaics (Hetsch et al., 2013; Kramer & Sargent, 2011; Wood & Bulović, 2010).

Methods for the generation of those quantum dots have been predominated and widely studied by solution processed methods. However, the requirement to handle costly and toxic metal-organic compounds, purity problems caused by the ligands and dispersants, and the complexity of the multi-step of the process act as drawbacks of liquid-based method for nanomaterial synthesis (Wegner & Pratsinis, 2005). On the other hand, aerosol-based gas phase

methods have some advantages since aerosol process generates much less byproducts than liquid-based methods and product collection and control is usually easier from gas than from liquid solution (Pratsinis, 2010).

Among those aerosol-based gas phase methods, generating nanoparticles using spark discharge have taken center stage since the simple, clean and energy efficient method which is carried out at atmospheric pressure and room temperature (Meuller et al., 2012; Schwyn et al., 1988; Tabrizi et al., 2009). This method can produce metal nanoparticles using various materials, and directly applied for the performance enhancement of nano-devices (Sung et al., 2014). Additionally, since the nanoparticles generated by the spark discharge generation are naturally charged by the spark plasma (Bau et al., 2010), it can be used as building blocks for controlled fabrication by electrical forces (Ha et al., 2016; Lee et al., 2010). However, materials applied to this technique have been usually restricted to the metal nanoparticles due to the necessity of high conductivity of electrode material. Such spark discharge generation technique is facile and adequate way for generating sub-10 nm nanoparticles (Meuller et al., 2012), it can be a powerful method for synthesizing semiconductor quantum dot with simple process and high purity.

In addition to the expansion of the diversity of producing materials, efficiency of particle production has crucial roles in nanoparticle utilization (Pfeiffer et al., 2014). Long-time durability and mass production of nanoparticles are essential elements for the practical use of spark generated

nanoparticles. To produce nanoparticles consistently and scale up the production rate, geometrical improvement of electrode structure can enhance the stability and the production of nanoparticles, which increase the usability of the spark discharge generation method in the industrial use.

1.2. Objective of Research

In this research, we pursue developing high efficient nanoparticle synthesis method for generating semiconductor nanoparticles using spark discharge. To achieve this objectives, we extend the material diversity of spark discharge generation method. From the conventional metal-oriented nanoparticle generation, the semiconductor materials were employed for the generation of quantum dots. In chapter 2, the production of silicon nanocrystals by hydrogen assisted spark discharge generation was investigated. Pure, crystalline, and hydrogen passivated silicon nanoparticles were generated introducing the hydrogen gas in the spark discharge system, which causes reducing atmosphere and hydrogen insertion-relaxation in the silicon particle matrix.

For the profound understanding of crystallization mechanism of the semiconductor nanoparticles in the spark discharge system, we studied the synthesizing of gallium arsenide nanocrystals by spark discharge generation, which is more complex process. In chapter 3, the crystallization mechanism and optical properties (especially quantum confinement effect) of gallium arsenide nanoparticles are investigated.

Moreover, the improvement of spark discharger for the efficient nanoparticle generation was studied. In chapter 4, a newly designed spark discharger exhibited the long-time consistent generation of nanoparticles. Integration of the merits of rod-to-rod spark discharger and pin-to=plate spark discharger

was required and it proved that particle size distributions of generated nanoparticles were maintained over 12 hours. Lastly, for the mass production of nanoparticles, we rapidly remove the residual plasma between spark electrodes and accomplished the stability of the high frequency spark discharge. Consequently, we confirmed that strong electric field from asymmetric electrode structure and fast flow rate of carrier gas in the spark zone enabled the high frequency of the spark discharge up to 20 kHz.

1.3. References

Atwater, H. A., & Polman, A. (2010). Plasmonics for improved photovoltaic devices. *Nature materials, 9*(3), 205.

Bau, S., Witschger, O., Gensdarmes, F., Thomas, D., & Borra, J.-P. (2010). Electrical properties of airborne nanoparticles produced by a commercial spark-discharge generator. *Journal of Nanoparticle Research, 12*(6), 1989-1995.

Daniel, M.-C., & Astruc, D. (2004). Gold nanoparticles: assembly, supramolecular chemistry, quantum-size-related properties, and applications toward biology, catalysis, and nanotechnology. *Chemical reviews, 104*(1), 293-346.

Ha, K., Jang, E., Jang, S., Lee, J.-K., Jang, M. S., Choi, H., Cho, J.-S., & Choi, M. (2016). A light-trapping strategy for nanocrystalline silicon thin-film solar cells using three-dimensionally assembled nanoparticle structures. *Nanotechnology, 27*(5), 055403.

Haes, A. J., & Van Duyne, R. P. (2002). A nanoscale optical biosensor: sensitivity and selectivity of an approach based on the localized surface plasmon resonance spectroscopy of triangular silver nanoparticles. *Journal of the American Chemical Society, 124*(35), 10596-10604.

Hetsch, F., Zhao, N., Kershaw, S. V., & Rogach, A. L. (2013). Quantum dot field effect transistors. *Materials Today, 16*(9), 312-325.

Karch, J., Birringer, R., & Gleiter, H. (1987). Ceramics ductile at low temperature. *Nature, 330*(6148), 556-558.

Kramer, I. J., & Sargent, E. H. (2011). Colloidal quantum dot photovoltaics: a path forward. *ACS nano, 5*(11), 8506-8514.

Kruis, F. E., Fissan, H., & Peled, A. (1998). Synthesis of nanoparticles in the gas phase for electronic, optical and magnetic applications—a review. *Journal of Aerosol Science, 29*(5), 511-535.

Lee, H., You, S., Pikhitsa, P. V., Kim, J., Kwon, S., Woo, C. G., & Choi, M. (2010). Three-dimensional assembly of nanoparticles from charged aerosols. *Nano letters, 11*(1), 119-124.

Meuller, B. O., Messing, M. E., Engberg, D. L., Jansson, A. M., Johansson, L. I., Norlén, S. M., Tureson, N., & Deppert, K. (2012). Review of spark discharge generators for production of nanoparticle aerosols. *Aerosol Science and Technology, 46*(11), 1256-1270.

Moras, J. D., Strandberg, B., Suc, D., & Wilson, K. (1996). Semiconductor clusters, nanocrystals, and quantum dots. *science*, *271*, 933.

Pfeiffer, T., Feng, J., & Schmidt-Ott, A. (2014). New developments in spark production of nanoparticles. *Advanced Powder Technology, 25*(1), 56-70.

Pratsinis, S. E. (2010). Aerosol- based technologies in nanoscale manufacturing: from functional materials to devices through core chemical engineering. *AIChE journal, 56*(12), 3028-3035.

Schwyn, S., Garwin, E., & Schmidt-Ott, A. (1988). Aerosol generation by spark discharge. *Journal of Aerosol Science, 19*(5), 639-642.

Siegel, R. W. (1993). Nanophase materials assembled from atom clusters. *Materials Science and Engineering: B, 19*(1-2), 37-43.

Sung, H., Lee, J., Han, K., Lee, J.-K., Sung, J., Kim, D., Choi, M., & Kim, C. (2014). Controlled positioning of metal nanoparticles in an organic light-emitting device for enhanced quantum efficiency. *Organic Electronics, 15*(2), 491-499.

Tabrizi, N. S., Ullmann, M., Vons, V., Lafont, U., & Schmidt-Ott, A. (2009). Generation of nanoparticles by spark discharge. *Journal of Nanoparticle Research, 11*(2), 315.

Wegner, K., & Pratsinis, S. E. (2005). Gas-phase synthesis of nanoparticles: scale-up and design of flame reactors. *Powder technology, 150*(2), 117-122.

Wood, V., & Bulović, V. (2010). Colloidal quantum dot light-emitting devices. *Nano reviews, 1*(1), 5202.

Chapter 2.

Hydrogen-assisted Spark Discharge Generation of Highly Crystalline and Surface-passivated Silicon Nanoparticles

2.1. Introduction

Spark discharge generation (Schwyn et al., 1988) has been well established as a simple and clean technique for generating sub-10nm nanoparticles among various synthesis methods. The nanoparticles produced by spark discharge generation can be directly incorporated into many electronic and optical devices without the need of any solution-based processing. For instance, spark discharge generated gold nanoparticles were embedded in organic display devices (Sung et al., 2014) to increase the quantum efficiency without appreciable damage of the underlying organic material, and gold seed nanoparticles were used for nanowire growth (Messing et al., 2009). In addition, spark discharge generation has been utilized to fabricate sophisticated three-dimensional nanostructures via ion-assisted aerosol lithography (Lee et al., 2010; You et al., 2010; Jung et al., 2014), as well as to enable the positioning of various charged nanoparticles at precise locations on a dielectric surface (Krinke et al., 2001). Furthermore, spark discharge generation is able to produce nanoparticles with complex compositions, such as bimetallic nanoparticles (Byeon et al., 2008) and composite nanoparticles (Kala et al., 2013).

Until now, spark discharge generation has been mainly used to produce metallic nanoparticles and the effects of process parameters on the generation process have been well understood. In contrast, spark discharge generation of non-metallic nanoparticles, such as those made of semiconducting materials,

have not been widely studied. A recent study regarding silicon nanoparticle generation showed that doped silicon electrodes can be used to enhance the production rate (Vons et al., 2011), but the generated silicon nanoparticles were agglomerated and gradually oxidized in air to some degrees. Since silicon nanoparticles have unique properties such as large volume change in lithiation and de-lithiation (Ding et al., 2009) and direct bandgap semiconducting behavior (Hirasawa et al., 2006), they have received much attention and have been used in various applications including Li-ion batteries (Ding et al., 2009), photoluminescence (Hua et al., 2006) and photovoltaics (Cabarrocas et al., 2004). The performance of these devices is greatly affected by the size, crystallinity, purity, and surface chemistry of the nanoparticles. Therefore, it is essential to fine-tune the production process to tightly control these properties.

Silicon nanoparticles have been produced by a variety of physical and/or chemical processes, including laser ablation of bulk silicon (Yoshida et al., 1996), nucleation in precursor solution (English et al., 2002), pyrolysis of gas phase precursor (Huisken et al., 2002), fracturing of electrochemically etched porous silicon (Lie et al., 2002), or even ball milling of graphite and silicon dioxide (Lam et al., 2000). Generally, gas phase production yields silicon nanoparticles with good size control, yet it is challenging to control their surface chemistry. On the other hand, liquid phase nucleation or electrochemical etching can achieve desired surface chemistry, but suffers

from either contamination or irregular shapes of the particles. Production of pure, crystalline, spherical, unagglomerated and surface passivated silicon nanoparticles has not been realized so far to the best of authors' knowledge.

Recently, *Hallberg et al*. have reported that by introducing a small amount of hydrogen into the spark discharge generator, small spherical metal nanoparticles were generated. One possible explanation for the spherical shape may be the absence of oxides acting as diffusion barriers leading to better particle coalescence (Hallberg et al., 2015). However, it would be also possible that hydrogen addition could influence the discharge characteristics. Hydrogen passivation is a commonly used technique to remove dangling bonds from silicon surfaces to prevent them from forming oxides, and hence the hydrogen-assisted spark discharge generation opens up an opportunity to passivate the silicon nanoparticles *in situ* as they are produced in the spark discharge chamber. In this study, we sought to produce unagglomerated and surface passivated silicon nanoparticles with improved purity and crystallinity by introducing hydrogen atmosphere into the spark discharge chamber.

2.2. Experimental Methods

The experimental setup consisting of a pin-to-plate spark discharge generator (Han et al., 2012), an electrostatic precipitator, high voltage power supplies and mass flow controllers are shown in Figure 2.1(a). The spark discharge generator was constructed using a cylindrical stainless steel chamber, silicon electrodes, electrode holders, and features an inlet and an outlet for carrier gas flow. The spark discharge generator and the electrostatic precipitator were installed in a glove box filled with nitrogen to prevent oxidation of the electrodes and the generated nanoparticles. High purity argon and hydrogen (99.999% purity) were mixed in varying ratios and used as the carrier gas. The gas flows were regulated by mass flow controllers, mixed with a static mixer and injected into the spark discharge generator. The total carrier gas flow was fixed at 3 lpm, and three different mixture ratios were used: pure argon, 1:1 argon and hydrogen, and pure hydrogen. A high-voltage DC power supply was used to apply 6 kV to the pin electrode through the external electric circuit consisting of a capacitor (2 nF) and a resistor (3 MΩ). The electrodes and the circuit were configured to maintain the discharge voltage at 3 kV and the spark frequency at 200 Hz by continuously adjusting the electrode gap distance, and these values were monitored using an oscilloscope (Agilent DSO-X 3014A) and a high voltage probe (Tektronix P6015A). Highly doped n-type silicon (3±0.1 mΩ·cm) was used as electrodes. The flow conditions and electrode material were chosen to ensure that the

spark current decays by damped harmonic oscillation (Figure 2.1(b)), which signifies that the spark energy is mostly used to ablate the electrode material instead of being dissipated in the electrodes, and this results in the increased silicon nanoparticle production rate (Vons et al., 2011).

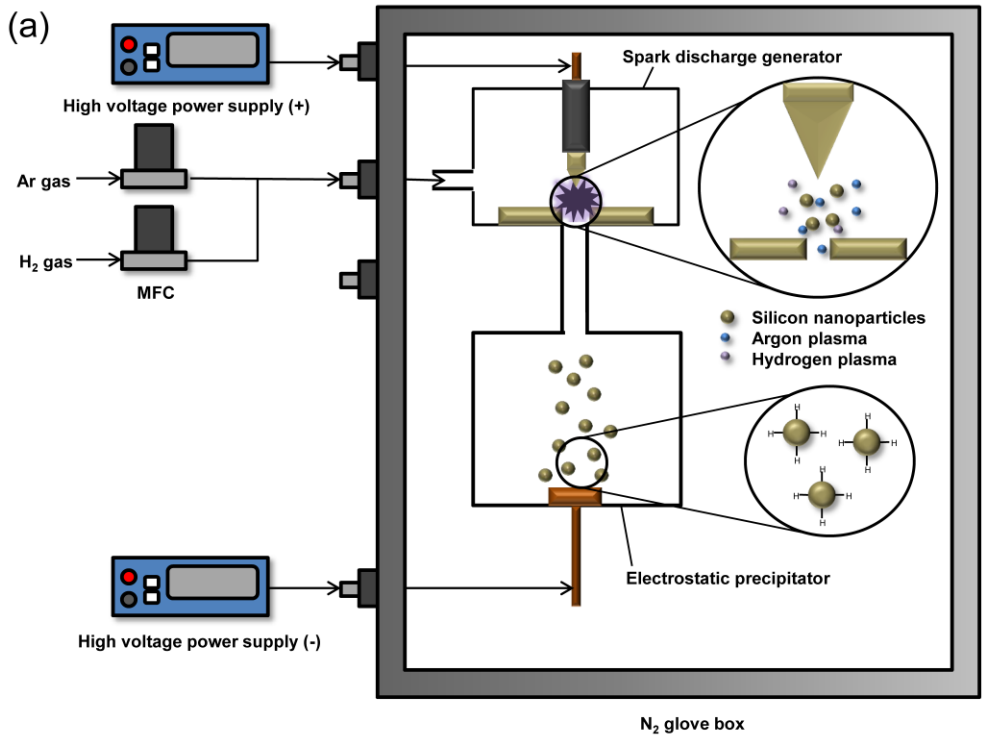

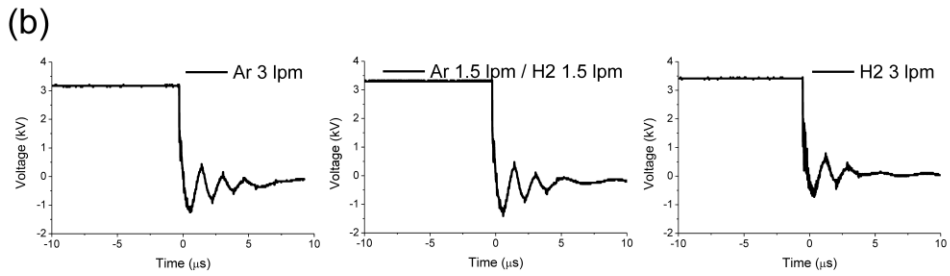

Figure 2.1. (a) A schematic of the experimental setup for spark discharge generation of silicon nanoparticles. (b) Voltage across the n-doped silicon electrodes during a spark discharge event in various carrier gas compositions

To characterize the morphology and the size distribution of generated silicon nanoparticles, high resolution transmission electron microscopy (HR-TEM, JEOL ARM 200F) with energy dispersive X-ray spectroscopy (EDS, X-max^N 80T) was carried out. Positively charged silicon nanoparticles were collected on a carbon film-coated copper TEM grid using an electrostatic precipitator by applying -3 kV DC bias for 5 minutes. The particles were collected after several hours of spark discharge operation to ensure that the oxide layers on the silicon electrodes have been ablated away. In addition, the crystallinity, oxidation states and surface chemistry of the nanoparticles were assessed by X-ray diffraction (XRD, Bruker New D8 Advance), Raman spectroscopy (Horiba Jobin-Yvon LabRam ARAMIS), and Fourier transform infrared spectroscopy (FT-IR, Bruker VERTEX80v) measurements, respectively. These measurements were performed on a porous film of nanoparticles (~8 μm thick after a 12 hour deposition) deposited on a silver substrate (99.99% purity, 0.5 mm thick).

2.3. Results and Discussion

HR-TEM images show that the nanoparticles generated in pure argon flow were generally agglomerated (Figure 2.2(a) left). The high magnification image (Figure 2.2(a) middle) reveals that both crystalline and amorphous silicon nanoparticles are present. EDS analysis show both silicon and oxygen peaks are present (Figure 2.3), meaning that at least some amorphous silicon oxide particles were generated (inset in Figure 2.2(a) middle). This signifies that even with inert argon atmosphere in the spark discharge generator, trace amounts of oxygen present in the system oxidizes the generated particles, and the spark energy was insufficient to form crystalline silicon nanoparticles (Hirasawa et al., 2006; Kramer et al., 2014). XRD measurements (Figure 2.2(a) right) show that Si (220) and Si (311) peaks are hardly present and there exists a shoulder at lower 2 theta range, confirming that particles generated were indeed amorphous. Here, the presence of Si (111) peak indicates that some crystalline particles were generated as observed in the TEM images. A reducing environment is needed to eliminate oxide particles and to enhance the crystallinity of the silicon nanoparticles, thus we introduced hydrogen in 1:1 mixing ratio with argon while keeping the total flow rate at 3 lpm. TEM images of generated particles in 1:1 hydrogen-argon environment (Figure 2.2(b) left, middle) show that almost all particles are crystalline and unagglomerated. The reducing atmosphere effectively eliminated the amorphous oxide particles. The size distributions of silicon nanoparticles

were estimated from 500 nanoparticles using projected area equivalent diameters (PAED), and the geometric mean diameter of generated silicon nanoparticles was 5.38 nm with a standard deviation of 1.34 nm (Figure 2.4(a)). XRD measurement (Figure 2.2(b), right) shows that the shoulder at low 2 theta is reduced, indicating that the amorphous nanoparticles were mostly removed. In addition, sharp peaks were observed at Si (111), Si (220) and Si (311), confirming that the presence of hydrogen in the carrier gas stream improved the crystallinity of generated silicon nanoparticles. Some mechanisms behind how the hydrogen plasma may lead to better crystallinity have been reported previously, and include Si-Si bond rearrangement by hydrogen insertion and relaxation (Sriraman et al., 2002) and plasma induced particle heating (Kramer et al., 2014). In a pure hydrogen environment, we observed that highly crystalline and unagglomerated silicon nanoparticles were generated (Figure 2.2(c) left, middle), and the geometric mean diameter and the geometric standard deviation were estimated to be 5.04 nm and 1.39 nm, respectively (Figure 2.4(b)), which signifies that the particle size distribution has not changed much from that of the 1:1 hydrogen-argon case. Lattice lines with a 3.15 Å spacing are visible in the TEM image, close to the theoretical value of 3.13 Å (Vons et al., 2011), and XRD (Figure 2.2(c), right) results show clear silicon peaks, confirming that the crystalline silicon nanoparticles were generated instead of amorphous silicon or silicon oxide particles.

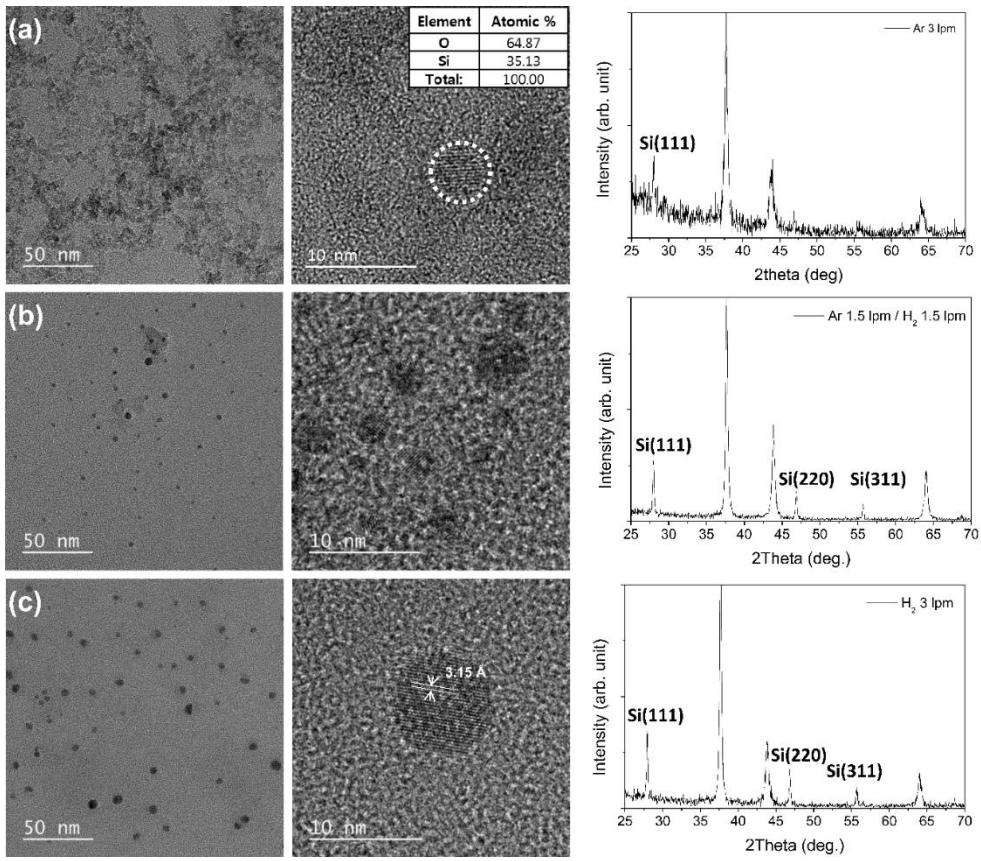

Figure 2.2. TEM images showing multiple particles at low magnification (left), individual particles at high magnification (middle) and XRD (right) of silicon nanoparticles generated in (a) Ar 3 lpm (inset in middle panel shows EDS data, full data shown in SI), (b) Ar 1.5 lpm/H_2 1.5 lpm, and (c) H_2 3 lpm.

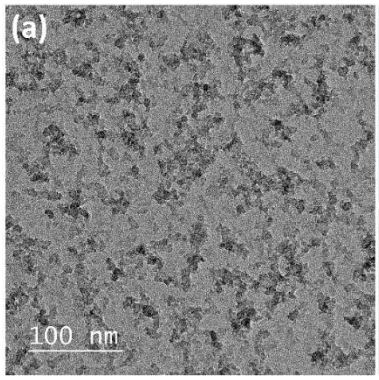

Element	Line Type	k Factor	k Factor type	Absorption Correction	Wt%	Wt% Sigma	Atomic %
O	K series	2.095		1.00	47.22	11.46	61.09
Si	K series	1.000		1.00	52.78	11.46	38.91
Total:					100.00		100.00

Figure 2.3. (a) TEM image and (b) EDS spectra of silicon nanoparticles generated in pure argon flow.

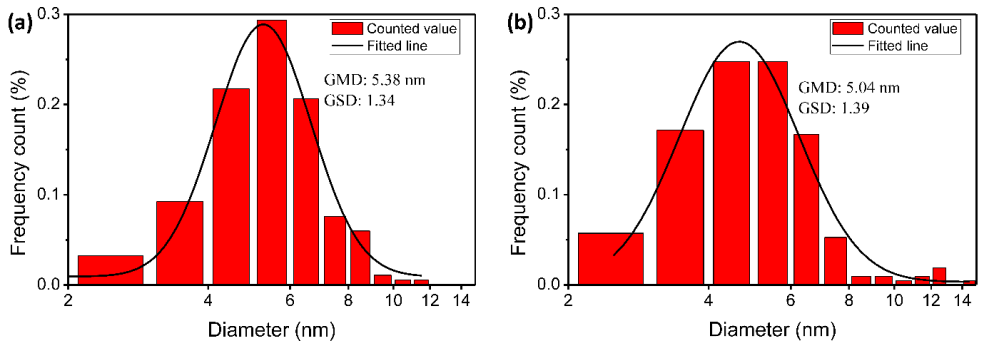

Figure 2.4. Size distribution of silicon nanoparticles generated in (a) Ar 1.5 lpm / H_2 1.5 lpm, and (b) H_2 3 lpm

Additionally, Raman spectroscopy was carried out to determine the presence of amorphous and/or crystalline silicon phases among the silicon nanoparticles produced in each carrier gas composition (Figure 2.5). The spectra were normalized to the silicon peak at 520 cm^{-1} for comparison. For particles generated with pure argon flow, a broad shoulder around 480 cm^{-1} and a sharp peak at 520 cm^{-1} are present, which correspond to amorphous and crystalline phases respectively. In contrast, the shoulder at 480 cm^{-1} is absent for particles generated with either 1:1 hydrogen-argon flow or pure hydrogen flow. These results confirm that less amorphous silicon particles were produced when the hydrogen gas was introduced.

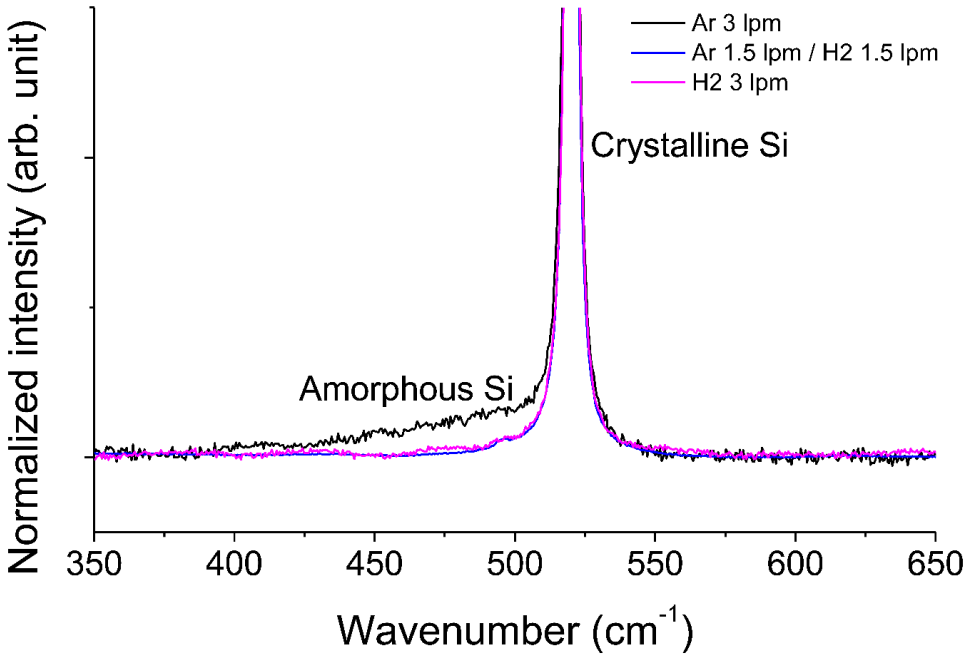

Figure 2.5. Raman spectra of spark discharge generated silicon nanoparticles using various carrier gas compositions. The spectra are normalized at 520 cm^{-1} (crystalline silicon) and zoomed into lower intensity values to clearly show the broad shoulder at 480 cm^{-1} (amorphous silicon).

Lastly, FT-IR measurements were performed to assess the purity and surface passivation of the particles. Figure 2.6(a) shows the wagging mode from Si-O bonds at 1100 cm^{-1} for particles produced in pure argon flow, which indicates the presence of silicon oxide particles among amorphous particles produced, in agreement with EDS results discussed earlier. The Si-O wagging mode is reduced for particles produced in 1:1 hydrogen-argon flow, and is further reduced for those produced in pure hydrogen. For these cases, deformation modes and stretching modes of $Si\text{-}H_x$ bonds are present instead. A number of symmetric deformation peaks around 850 cm^{-1} from SiH_3 and wagging peaks from SiH_2 were observed (Figure 2.6(b)) and the intensity of these peaks are higher for particles produced in pure hydrogen. $Si\text{-}H_x$ stretching modes around 2100 cm^{-1} follow similar trends (Figure 2.6(c)). The observed peaks associated with the deformation modes and stretching modes of $Si\text{-}H_x$ bonds are broad, indicating that there is no preference between SiH, SiH_2 and SiH_3 when hydrogen passivation occurs (Holm & Roberts, 2007). These results show that surface passivated silicon nanoparticles are produced when hydrogen is present in the atmosphere during the spark discharge process, and higher hydrogen content in the atmosphere leads to better surface passivation which leads to the less adhesion between silicon nanoparticles (Hawa & Zachariah, 2004).

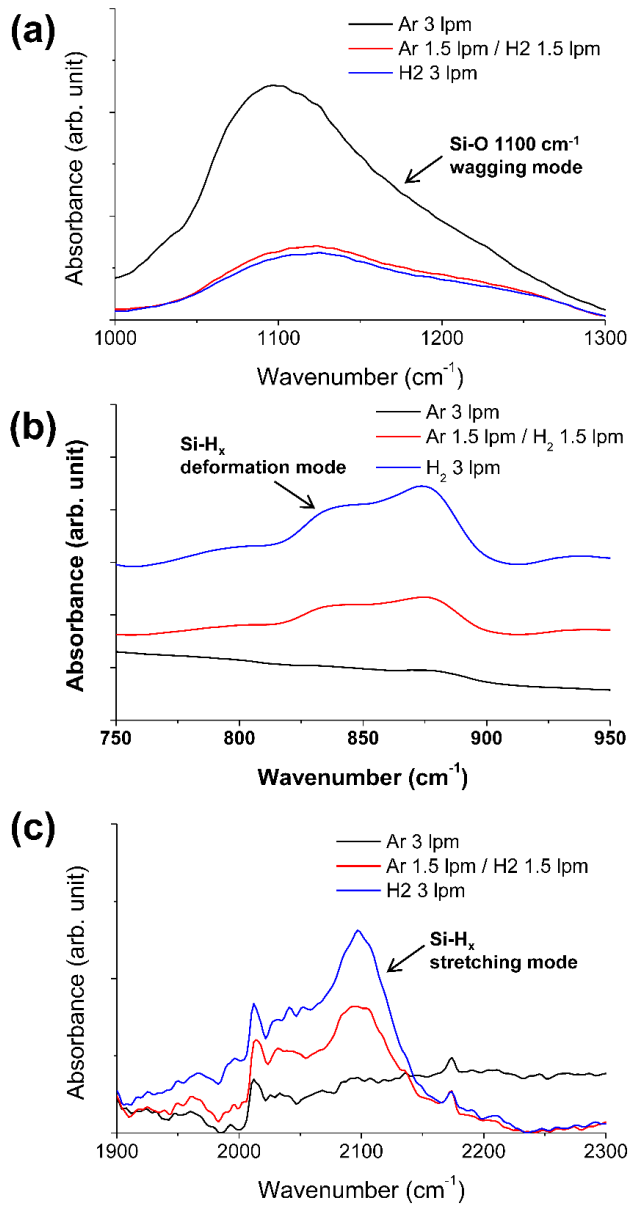

Figure 2.6. FT-IR absorption spectra of spark discharge generated silicon nanoparticles using various carrier gas compositions: (a) Si-O vibrational mode at 1100 cm^{-1}. (b) Si-H_x deformation modes at 850 – 900 cm^{-1}. (c) Si-H_x stretching modes at 2100 – 2200 cm^{-1}

2.4. Conclusion

We have successfully incorporated a reducing environment into the spark discharge generation process of silicon nanoparticles by injecting hydrogen into the carrier gas stream. The silicon oxide particles originating from trace amounts of oxygen in the system were eliminated by the presence of hydrogen. The produced particles possess improved crystallinity as observed in the TEM images, XRD and Raman spectra. FT-IR measurements showed that the peaks associated with Si-O wagging modes have lower intensity when hydrogen was injected into the carrier gas flow, which means that the generation of silicon oxide nanoparticles is suppressed. Simultaneously, peaks associated with deformation and stretching modes of Si-H_x bonds increased in intensity as the hydrogen content in the carrier gas increased, indicating better surface passivation. Hence, it can be concluded that the hydrogen-assisted spark discharge generation technique presented here is a facile way to produce highly crystalline and pure silicon particles with hydrogen-passivated surfaces, which have potential applications as silicon quantum dots in luminescence devices.

2.5. References

Byeon, J. H., Park, J. H., & Hwang, J. (2008). Spark generation of monometallic and bimetallic aerosol nanoparticles. *Journal of Aerosol Science, 39*(10), 888-896.

Cabarrocas, P. R., Chaabane, N., Kharchenko, A., & Tchakarov, S. (2004). Polymorphous silicon thin films produced in dusty plasmas: Application to solar cells. *Plasma physics and controlled fusion, 46*(12B), B235.

Ding, N., Xu, J., Yao, Y., Wegner, G., Lieberwirth, I., & Chen, C. (2009). Improvement of cyclability of Si as anode for Li-ion batteries. *Journal of power sources, 192*(2), 644-651.

English, D. S., Pell, L. E., Yu, Z., Barbara, P. F., & Korgel, B. A. (2002). Size tunable visible luminescence from individual organic monolayer stabilized silicon nanocrystal quantum dots. *Nano Letters, 2*(7), 681-685.

Hallberg, R. T., Dick, K. A., Magnusson, M. H., & Messing, M. E. (2015). *Hydrogen assisted generation and reshaping of metal particles by spark discharge.* Paper presented at the 2015 European Aeorol Conference, Millan, Italy.

Han, K., Kim, W., Yu, J., Lee, J., Lee, H., Woo, C. G., & Choi, M. (2012). A study of pin-to-plate type spark discharge generator for producing unagglomerated nanoaerosols. *Journal of Aerosol Science, 52*, 80-88.

Hawa, T., & Zachariah, M. (2004). Molecular dynamics study of particle–particle collisions between hydrogen-passivated silicon nanoparticles. *Physical Review B, 69*(3), 035417.

Hirasawa, M., Orii, T., & Seto, T. (2006). Size-dependent crystallization of Si nanoparticles. *Applied physics letters, 88*(9), 093119.

Holm, J., & Roberts, J. T. (2007). Surface chemistry of aerosolized silicon nanoparticles: Evolution and desorption of hydrogen from 6-nm diameter particles. *Journal of the American Chemical Society, 129*(9), 2496-2503.

Hua, F., Erogbogbo, F., Swihart, M. T., & Ruckenstein, E. (2006). Organically capped silicon nanoparticles with blue photoluminescence prepared by hydrosilylation followed by oxidation. *Langmuir, 22*(9), 4363-4370.

Huisken, F., Ledoux, G., Guillois, O., & Reynaud, C. (2002). Light-emitting silicon nanocrystals from laser pyrolysis. *Advanced Materials, 14*(24), 1861-1865.

Jung, K., Hahn, J., In, S., Bae, Y., Lee, H., Pikhitsa, P. V., Ahn, K., Ha, K., Lee, J. K., & Park, N. (2014). Hotspot-Engineered 3D Multipetal Flower Assemblies for Surface-Enhanced Raman Spectroscopy. *Advanced Materials, 26*(34), 5924-5929.

Kala, S., Theissmann, R., & Kruis, F. E. (2013). Generation of AuGe nanocomposites by co-sparking technique and their

photoluminescence properties. *Journal of nanoparticle research, 15*(9), 1-12.

Kramer, N., Anthony, R., Mamunuru, M., Aydil, E., & Kortshagen, U. (2014). Plasma-induced crystallization of silicon nanoparticles. *Journal of Physics D: Applied Physics, 47*(7), 075202.

Krinke, T. J., Fissan, H., Deppert, K., Magnusson, M. H., & Samuelson, L. (2001). Positioning of nanometer-sized particles on flat surfaces by direct deposition from the gas phase. *Applied Physics Letters, 78*(23), 3708-3710.

Lam, C., Zhang, Y., Tang, Y., Lee, C., Bello, I., & Lee, S. (2000). Large-scale synthesis of ultrafine Si nanoparticles by ball milling. *Journal of crystal growth, 220*(4), 466-470.

Lee, H., You, S., Pikhitsa, P. V., Kim, J., Kwon, S., Woo, C. G., & Choi, M. (2010). Three-dimensional assembly of nanoparticles from charged aerosols. *Nano letters, 11*(1), 119-124.

Lie, L. H., Duerdin, M., Tuite, E. M., Houlton, A., & Horrocks, B. R. (2002). Preparation and characterisation of luminescent alkylated-silicon quantum dots. *Journal of Electroanalytical Chemistry, 538*, 183-190.

Messing, M. E., Dick, K. A., Wallenberg, L. R., & Deppert, K. (2009). Generation of size-selected gold nanoparticles by spark discharge—for growth of epitaxial nanowires. *Gold Bulletin, 42*(1), 20-26.

Schwyn, S., Garwin, E., & Schmidt-Ott, A. (1988). Aerosol generation by

spark discharge. *Journal of Aerosol Science, 19*(5), 639-642.

Sriraman, S., Agarwal, S., Aydil, E. S., & Maroudas, D. (2002). Mechanism of hydrogen-induced crystallization of amorphous silicon. *Nature, 418*(6893), 62-65.

Sung, H., Lee, J., Han, K., Lee, J.-K., Sung, J., Kim, D., Choi, M., & Kim, C. (2014). Controlled positioning of metal nanoparticles in an organic light-emitting device for enhanced quantum efficiency. *Organic Electronics, 15*(2), 491-499.

Vons, V. A., de Smet, L. C., Munao, D., Evirgen, A., Kelder, E. M., & Schmidt-Ott, A. (2011). Silicon nanoparticles produced by spark discharge. *Journal of Nanoparticle Research, 13*(10), 4867-4879.

Yoshida, T., Takeyama, S., Yamada, Y., & Mutoh, K. (1996). Nanometer-sized silicon crystallites prepared by excimer laser ablation in constant pressure inert gas. *Applied Physics Letters, 68*(13), 1772-1774.

You, S., Han, K., Kim, H., Lee, H., Woo, C. G., Jeong, C., Nam, W., & Choi, M. (2010). High-Resolution, Parallel Patterning of Nanoparticles via an Ion-Induced Focusing Mask. *small, 6*(19), 2146-2152.

Chapter 3.

Gas-phase Synthesis of Gallium Arsenide Nanocrystals through Hydrogen Insertion and Relaxation by Spark Discharge

3.1. Introduction

Gallium arsenide is obviously the representative material of the III-V semiconductor family for its excellent electronic and optical properties (Adachi, 2009). Gallium arsenide has clearly exhibited in various optical and electrical devices in the highest level, such as photovoltaics (Green et al., 2015), transistors (Kroemer, 1982) and LEDs (Schubert et al., 2005) for the direct band gap of 1.42 eV and high electron mobility about 8500 $cm^2V^{-1}s^{-1}$. And its large Bohr exciton radius of 10 nm can lead to the strong quantum confinement effect in sub-10 nm gallium arsenide nanocrystals (GaAs quantum dots), which can absorb and emit the visible light (Brus, 1984). Up to now, nanostructures of the gallium arsenide have been generally fabricated by the vacuum process such as molecular beam epitaxy (MBE) (Stievater et al., 2001) or metal-organic chemical vapor deposition (MOCVD) (Li et al., 2000). However, these methods have critical drawbacks such as the usage of the toxic precursor such as arsine (AsH_3), the high degree of vacuum in process and limited use in film formation. Therefore simpler and more processible method is needed for the various applications of GaAs quantum dots (QDs). Recently, there were many studies to synthesize the GaAs quantum dots using colloidal methods, which used dehalosilylation reaction (Wells et al., 1989), transmetalation route (Lauth et al., 2012) and cation exchange (Beberwyck & Alivisatos, 2012). However, the crystallinity was poor or the impurities like byproducts act as drawback to the GaAs NCs.

The difficulties and disadvantages of colloidal synthesis of GaAs NCs can be resolved by aerosol method which is consisted of clean and simple process. Among various aerosol processes, spark discharge generation have been spotlighted for generating sub-10 nm charged aerosols (Meuller et al., 2012), which are liable to control and collect nanoparticles by electrical force (Krinke et al., 2001).Moreover, all process of spark discharge system occurs in the atmospheric pressure and generating condition is controllable without difficulty (Tabrizi et al., 2009). Therefore, the spark discharge method can be an effective way for generating GaAs NCs without hazardous precursors and impurities.

Herein, we studied a new synthetic process for the GaAs NCs with spark discharge generation. By using mechanically processed GaAs ingot as spark electrodes, stoichiometry of supplied precursors was ideally fulfilled. Since the III-V semiconductor NCs have more covalent and oxidative characteristic than Ⅱ-Ⅵ semiconductor NCs, highly reducing environment is necessary (Jones, 1997). Generally the hydrogen is a representative matter for the reduction and hydrogen atoms in the matrix of covalent bonded material can be enhance the crystallinity through bond rearrangement by hydrogen insertion and relaxation (Valipa et al., 2006). Therefore we introduced hydrogen gas in the spark discharge system for the above statements breaking from the conventional method which usually employ inert gas condition. Through this newly designed spark discharge system, we sought to produce

unagglomerated gallium arsenide nanoparticles with improved purity and crystallinity.

3.2. Experimental Methods

The experimental setup consisting of a pin-to-plate spark discharge generator (Han et al., 2012), tube furnaces, an electrostatic precipitator, high voltage power supplies and mass flow controllers are depicted in Figure 3.1. The spark discharge generator was designed and manufactured using a cylindrical stainless steel chamber, electrode holders, and features of an inlet and an outlet for carrier gas flow. Highly pure argon and hydrogen gas (99.999 % purity) were mixed in various ratios and used as a carrier gas. The gas flows were controlled by the mass flow controllers, mixed with a static mixer and injected into the inlet of spark discharger. High-voltage DC power supplies were used to apply high voltage for the spark discharge between GaAs electrodes and electrostatic precipitation of generated aerosols. In the spark discharger, voltage was applied to the pin electrode through the external electric circuit consisting of a capacitor and a resistor. The capacitance and resistance from the external circuit and the distance between the pin and the plate electrodes were regulated to vary spark condition such as breakdown voltage, frequency, and spark energy. Since the spark conditions affect the vaporization and nucleation of the gallium arsenide target, precise control of those parameters was important factor for the size control of generated GaAs NCs. And these values were monitored using an oscilloscope (Agilent DSOX-3014A) and a high voltage probe (Tektronix P6015A). Highly doped n-type GaAs was used as electrodes since the high electric conductivity was

needed to ensure that the spark current decays by damped harmonic oscillation, which assure that the spark energy is mostly used to vaporize the electrode material instead of being dissipated in the electrodes (Vons et al., 2011). A couple of tube furnaces was installed and connected to the outlet of the spark discharger to provide thermal energy to the generated GaAs nanoparticles.

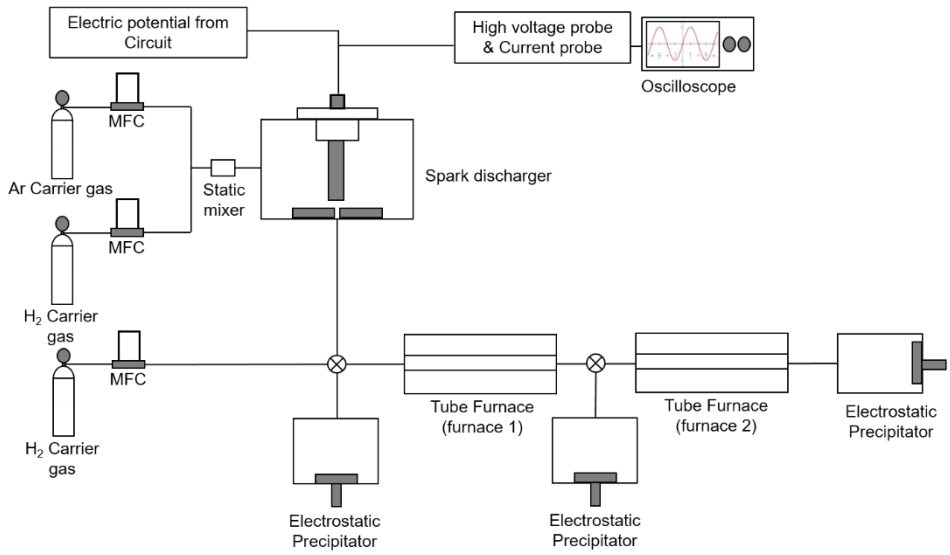

Figure 3.1. Experimental setup for generating crystalline gallium arsenide nanoparticles and particle collecting system.

To characterize the crystallinity, morphology and size distribution of generated GaAs nanoparticles, high resolution transmission electron microscopy (HR-TEM, JEOL ARM 200F) with energy dispersive X-ray spectroscopy (EDS, X-max^N 80T) was carried out. Positively charged GaAs nanoparticles were collected on a carbon film-coated TEM grid using an electrostatic precipitator by applying -2 kV DC bias for 3 minutes. Additionally, the crystallinity, defect abundancy, surface chemistry and optical properties of the nanoparticles were studied by X-ray diffraction (XRD, Bruker New D8 Advance), Raman spectroscopy (Horiba Jobin-Yvon LabRan ARAMIS), and Fourier transform infrared spectroscopy (FT-IR, Bruker VERTEX80v) measurements, respectively. These measurements were carried out on a porous film of GaAs nanoparticles (~3 μm thick after a 3 hour deposition) deposited on an ITO/glass substrate.

3.3. Results and Discussion

For observing the morphology of the spark-generated GaAs nanoparticles, we firstly carried out the HR-TEM measurement. As shown in Figure 3.2(a), in the condition of pure argon gas flow, highly agglomerated particles were generated and the crystallinity of the particles was poor (Figure 3.2(b)). Supporting this TEM results, in Figure 3.2(c), X-ray diffraction pattern shows that synthesized nanoparticles in this condition were amorphous. Inert atmosphere in the spark chamber caused the insufficient crystallization of generated nanoparticles and oxidation reaction would occur by the small amount of oxygen gas in the system (Lee et al., 2017). To form the reducing environment in the spark discharge chamber, 1 lpm of hydrogen gas was introduced instead of argon gas and total flow rate was maintained at 3 lpm (mixture gas condition). Figure 3.2(d) shows that agglomeration of the generated GaAs particles slightly lowered compared to the particles produced in the pure argon carrier gas which means the reluctant force between particles by the hydrogen adsorption (Hawa & Zachariah, 2004). However, just developing the reducing atmosphere was not satisfactory to enhance the crystallinity of the generated GaAs aerosols (Figure 3.2(e) and (f)). Since the hydrogen relaxation reaction from the inside of the GaAs particles matrix to the surface of the particles requires the energy contrary to the similar reaction in the silicon matrix (Lüth & Matz, 1981), we applied heat energy to the as-generated GaAs aerosols through the tube furnace (furnace 1).

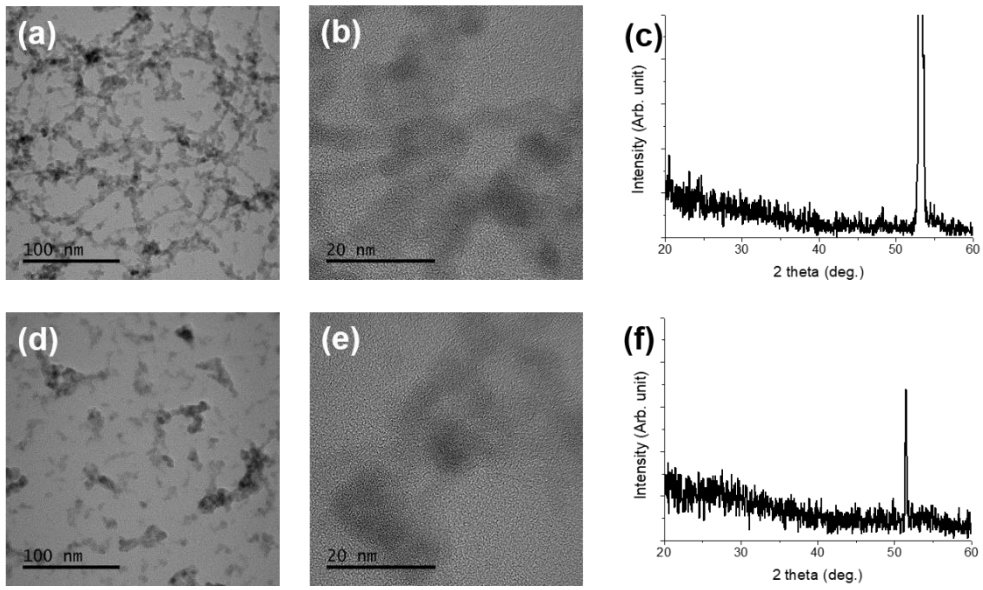

Figure 3.2. Results of generated GaAs particles in room temperature condition. (a)(b) TEM images of GaAs particles generated under 3 lpm of argon gas condition. (c) X-ray diffraction data of GaAs particles generated under argon 3 lpm gas condition. (d)(e) TEM images of GaAs particles generated under 2 lpm of argon and 1 lpm of hydrogen gas condition. (f) X-ray diffraction data of GaAs particles generated under 2 lpm of argon and 1 lpm of hydrogen gas condition.

HR-TEM images showed that un-agglomerated GaAs nanoparticles were obtained in Figure 3.3(a). In the inset of the Figure 3.3(a), the SAED pattern reveals that the generated nanoparticles have identical lattice lengths of 3.27 Å , 2.00 Å , and 1.71 Å , which coincide with theoretical value of GaAs lattice length. In figure 3.3(b), in high magnification image, core-shell type nanoparticles were confirmed which composed of GaAs nanocrystals and amorphous shells. XRD measurement was agreed with this core-shell particles, since the three crystalline peaks from the GaAs nanocrystals and a shoulder at low two theta range from the amorphous shells were both observed (Figure 3.3(c)).

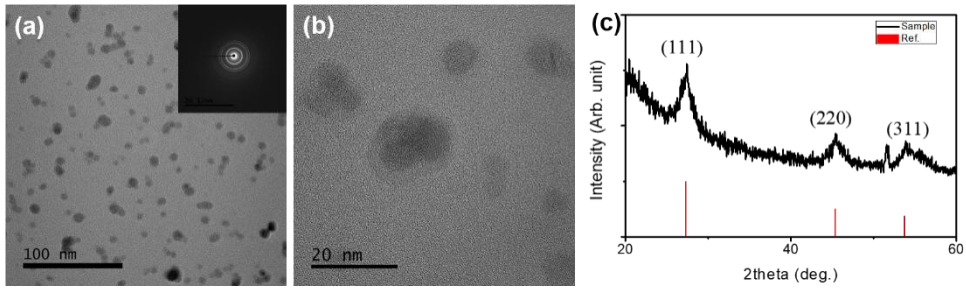

Figure 3.3. Results of generated GaAs particles annealed after spark discharge generation. (a)(b) TEM images of GaAs particles annealed at 950℃ after generated under 2 lpm of argon gas and 1 lpm of hydrogen gas condition. (c) X-ray diffraction data of GaAs particles annealed at 950℃ after generated under 2 lpm of argon gas and 1 lpm of hydrogen gas condition.

For the profound understanding of these crystallization phenomena of GaAs nanoparticles, FT-IR measurements were performed. We compared three nanoparticle samples generated in the condition of pure 3 lpm of argon gas, mixture gas, and 950 ℃-sintered mixture gas since both hydrogen gas and thermal energy were affected the crystallization of generated GaAs aerosols. Overall results were shown in Figure 3.4(a), and stretching mode from gallium-hydrogen bonds around wavenumber of 1720 cm^{-1} was depicted in Figure 3.4(b) (Wang et al., 1982). Strong absorption from Ga-H stretching modes were detected in the case of mixture gas condition contrast to the pure argon gas condition, which means the hydrogen gas was effectively dissociated and inserted in the GaAs matrix during the GaAs nanoparticle formation. Since the crystallinity of nanoparticles generated in this condition was absent, hydrogen atoms existed in the amorphous GaAs nanoparticles, and Ga-H bonds formed in those particles resulted in the FT-IR absorption spectra. Nanoparticles generated in the 950 ℃-sintered condition also revealed that Ga-H bonds were still maintained, which means hydrogen atoms successfully came out from the inside of particles to the surfaces of particles since the TEM images and XRD data indicated that synthesized particles were crystalline. Hydrogen atoms triggered the crystallization of GaAs nanoparticles in the process of bond relaxation which enabled by undergoing the thermal energy. Once the hydrogen bonds were broken and after hydrogen atoms moved away from the bond-centered location, the strained Ga-As

bonds underwent local structural rearrangements that resulted in bond lengths and angles closer to those of crystalline GaAs (Sriraman et al., 2002).

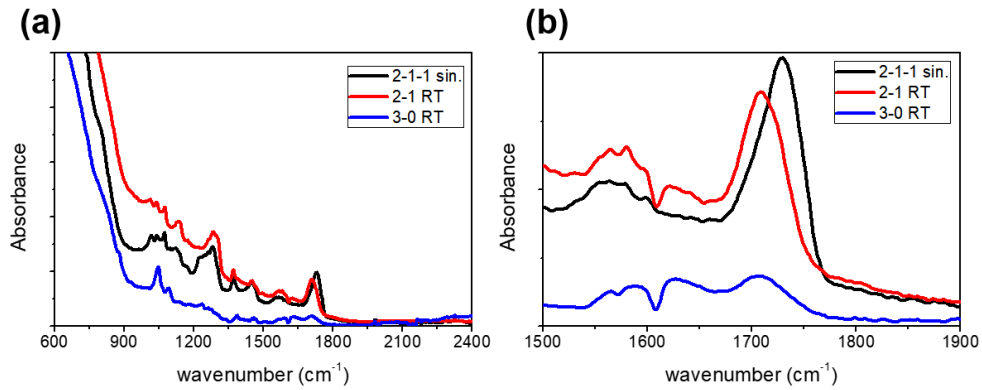

Figure 3.4. Identification of hydrogen atom insertion into GaAs bonding through Fourier transform infrared spectroscopy. Peak at 1720 cm^{-1} indicates Ga-H stretching modes.

For higher crystallinity like curing defects or removing anti-sites, we applied additional tube furnace (furnace 2) for the rearrangement of local structure. Since the GaAs bulk material was used as precursor material, supplied amounts of gallium and arsine were similar. Thus, additional thermal sintering was sufficient to improve crystallinity of generated GaAs NCs. TEM measurement and Raman spectroscopy were used to characterize the removal of amorphous shell around NCs and defect curing. As shown in Figure 3.5(a), amorphous shells surrounding GaAs NCs were clearly observed in high magnification image, which means crystallization process through hydrogen relaxation was not fully proceeded and hydrogen atoms might be remained in the amorphous shell. Raman spectroscopy on these nanoparticles showed a broad feature around wavenumber of 250 cm^{-1} and did not show characteristic LO and TO phonon modes at wavenumber of 265 cm^{-1} and 285 cm^{-1} (Figure 3.5(b)). Such Raman features point to a significant disorder in the lattice of GaAs NCs (Srivastava et al., 2017), even if the crystalline nanoparticles were observed in TEM images. The temperature of furnace 2 was set to 500 ℃ and 700 ℃, since higher temperature above 700 ℃ causes arsenic losses which debases the crystallinity of NCs (Creighton, 1990). In Figure 3.5(c), in the TEM image of nanoparticles additionally annealed at 500 ℃, shell thickness decreased from ~2.3 nm to ~1.1 nm, which reveals amorphous shells effectively crystallized through furnace 2. TO phonon mode at wavenumber of 285 cm^{-1} started to appear but the heat energy was insufficient to cure the

defect site or anti-site of inner GaAs NCs as shown in Raman spectra (Figure 3.5(d)). Particle image depicted in Figure 3.5(e) showed that amorphous shells around NCs were hardly present, which supported by Raman spectra showing clear LO and TO phonon modes of GaAs (Figure 3.6(f)).

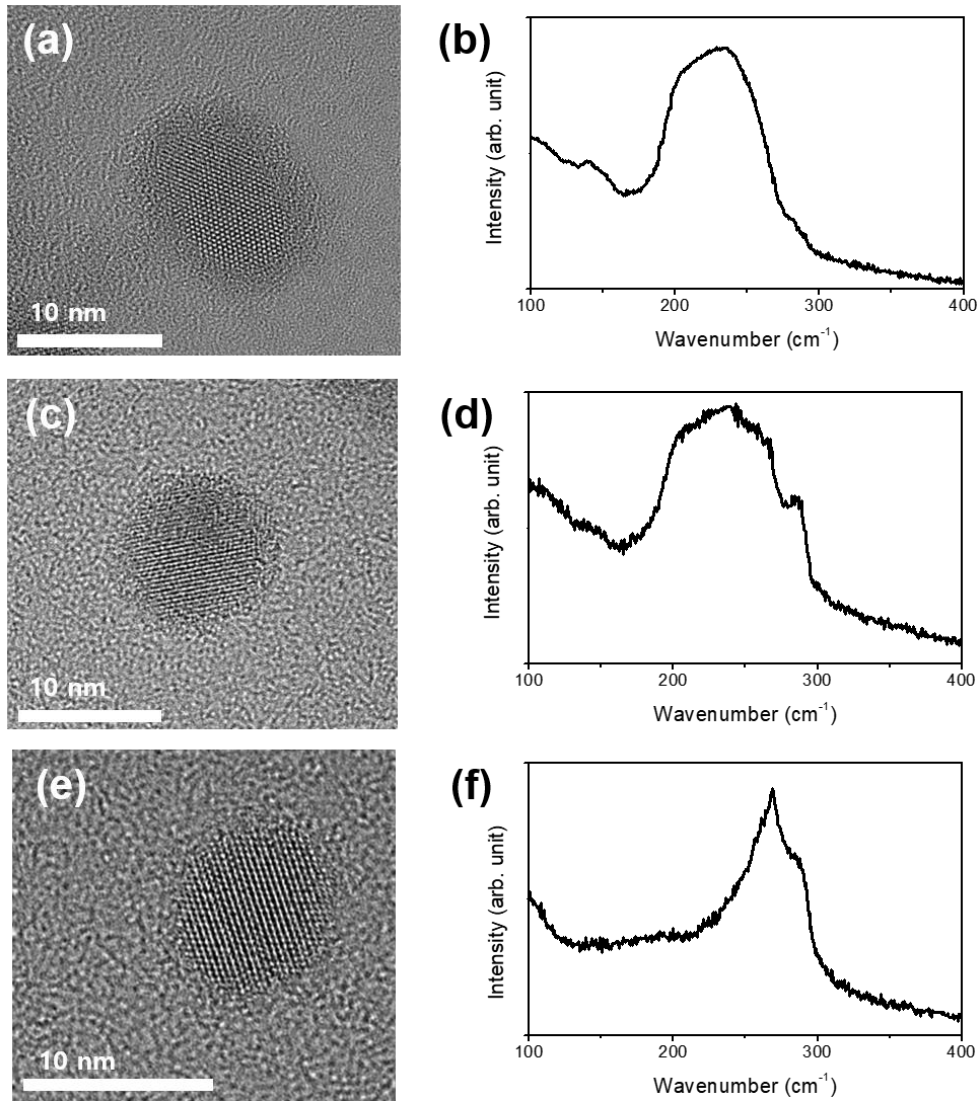

Figure 3.5. Decreasing shell thickness and enhancement of crystallinity of GaAs nanocrystals through introducing additional annealing of generated GaAs NCs with different temperature. High magnification TEM image and raman spectra of (a)(b) without additional annealing (c)(d) with temperature of 500 ℃, and (e)(f) 700 ℃.

After successfully obtain highly crystallized GaAs nanoparticles, we measured the photoluminescence to analyze the quantum confinement effect of generated GaAs NCs. To confirm the quantum confinement effect, we need to control the crystal size of particles. Spark energy, which is calculated by equation of $E_{spark} = 1/2\ C_{ext}V_{discharge}^2$ (Tabrizi et al., 2009), was regulated by adjusting external capacitance and spark frequency was controlled by external resistance for un-agglomerated nanoparticle generation. As shown in Figure 3.6, nanocrystals with various emission of photoluminescence in visible light area were obtained by controlling their size, which revealed the energy bandgap of NCs increased as decreasing of particle size.

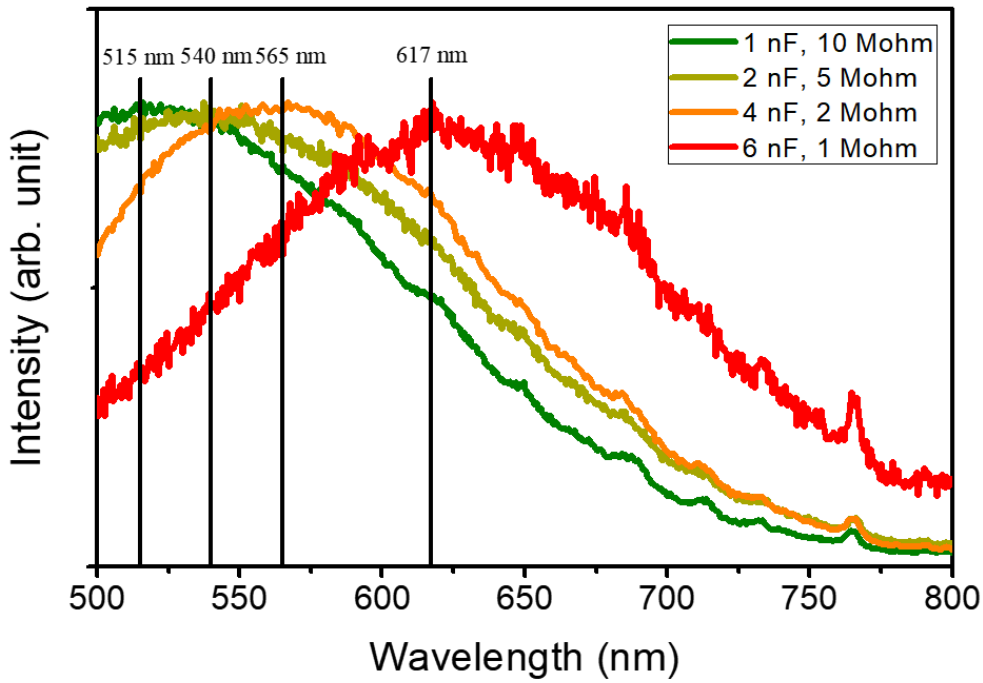

Figure 3.6. Photoluminescence spectra of GaAs nanocrystals with various sizes.

3.4. Conclusion

In this study, we have successfully applied hydrogen assisted spark discharge generation into the synthesis of gallium arsenide nanocrystals. Crystalline GaAs nanoparticles were generated by hydrogen insertion and relaxation mechanism, which enabled Ga-As bonds to undergo local structural arrangement. Inserted hydrogen atoms by spark discharge were relaxed through thermal annealing since hydrogen relaxation from GaAs particle matrix required additional energy. Through the TEM, XRD, and FT-IR measurement, we confirmed that Ga-H bonds were both detected before and after thermal sintering, which revealed hydrogen atoms inside the GaAs particle matrix successfully escaped to the surfaces of particles. For the higher crystallinity of GaAs NCs, serial thermal annealing was applied, which confirmed by TEM measurement and Raman spectra. Shell thickness decrement and appearance of LO and TO phonon modes of particles indicates the defects and anti-sites of generated particles were effectively cured. To identify the quantum confinement effect of generated GaAs NCs, particle size controls by adjusting spark energy and frequency were carried out and emission wavelengths were variously controlled by regulating crystal size, which are applicable to GaAs quantum dots and luminescence devices.

3.5. References

Adachi, S. (2009). *Properties of semiconductor alloys: group-IV, III-V and II-VI semiconductors* (Vol. 28): John Wiley & Sons.

Beberwyck, B. J., & Alivisatos, A. P. (2012). Ion exchange synthesis of III–V nanocrystals. *Journal of the American Chemical Society, 134*(49), 19977-19980.

Brus, L. E. (1984). Electron–electron and electron- hole interactions in small semiconductor crystallites: The size dependence of the lowest excited electronic state. *The Journal of chemical physics, 80*(9), 4403-4409.

Creighton, J. (1990). Hydrogen chemisorption and reaction on GaAs (100). *Journal of Vacuum Science & Technology A: Vacuum, Surfaces, and Films, 8*(6), 3984-3987.

Green, M. A., Emery, K., Hishikawa, Y., Warta, W., & Dunlop, E. D. (2015). Solar cell efficiency tables (version 46). *Prog. Photovoltaics, 23*(7), 805-812.

Han, K., Kim, W., Yu, J., Lee, J., Lee, H., Woo, C. G., & Choi, M. (2012). A study of pin-to-plate type spark discharge generator for producing unagglomerated nanoaerosols. *Journal of Aerosol Science, 52*, 80-88.

Hawa, T., & Zachariah, M. (2004). Molecular dynamics study of particle–particle collisions between hydrogen-passivated silicon nanoparticles. *Physical Review B, 69*(3), 035417.

Jones, A. C. (1997). Developments in metalorganic precursors for

semiconductor growth from the vapour phase. *Chemical Society Reviews, 26*(2), 101-110.

Krinke, T. J., Fissan, H., Deppert, K., Magnusson, M. H., & Samuelson, L. (2001). Positioning of nanometer-sized particles on flat surfaces by direct deposition from the gas phase. *Applied Physics Letters, 78*(23), 3708-3710.

Kroemer, H. (1982). Heterostructure bipolar transistors and integrated circuits. *Proceedings of the IEEE, 70*(1), 13-25.

Lauth, J., Strupeit, T., Kornowski, A., & Weller, H. (2012). A Transmetalation Route for Colloidal GaAs Nanocrystals and Additional III–V Semiconductor Materials. *Chemistry of Materials, 25*(8), 1377-1383.

Lee, D., Lee, K., Kim, D. S., Lee, J.-K., Park, S. J., & Choi, M. (2017). Hydrogen-assisted spark discharge generation of highly crystalline and surface-passivated silicon nanoparticles. *Journal of Aerosol Science, 114*, 139-145.

Li, R., Dapkus, P., Thompson, M. E., Jeong, W., Harrison, C., Chaikin, P., Register, R., & Adamson, D. (2000). Dense arrays of ordered GaAs nanostructures by selective area growth on substrates patterned by block copolymer lithography. *Applied Physics Letters, 76*(13), 1689-1691.

Lüth, H., & Matz, R. (1981). Hydrogen adsorption on GaAs (110) studied by electron-energy-loss spectroscopy. *Physical Review Letters, 46*(25),

1652.

Meuller, B. O., Messing, M. E., Engberg, D. L., Jansson, A. M., Johansson, L. I., Norlén, S. M., Tureson, N., & Deppert, K. (2012). Review of spark discharge generators for production of nanoparticle aerosols. *Aerosol Science and Technology, 46*(11), 1256-1270.

Schubert, E. F., Gessmann, T., & Kim, J. K. (2005). *Light emitting diodes*: Wiley Online Library.

Sriraman, S., Agarwal, S., Aydil, E. S., & Maroudas, D. (2002). Mechanism of hydrogen-induced crystallization of amorphous silicon. *Nature, 418*(6893), 62.

Srivastava, V., Liu, W., Janke, E. M., Kamysbayev, V., Filatov, A. S., Sun, C.-J., Lee, B., Rajh, T., Schaller, R. D., & Talapin, D. V. (2017). Understanding and curing structural defects in colloidal GaAs nanocrystals. *Nano Letters, 17*(3), 2094-2101.

Stievater, T., Li, X., Steel, D. G., Gammon, D., Katzer, D., Park, D., Piermarocchi, C., & Sham, L. (2001). Rabi oscillations of excitons in single quantum dots. *Physical Review Letters, 87*(13), 133603.

Tabrizi, N. S., Ullmann, M., Vons, V., Lafont, U., & Schmidt-Ott, A. (2009). Generation of nanoparticles by spark discharge. *Journal of Nanoparticle Research, 11*(2), 315.

Valipa, M. S., Sriraman, S., Aydil, E. S., & Maroudas, D. (2006). Hydrogen-induced crystallization of amorphous Si thin films. II. Mechanisms

and energetics of hydrogen insertion into Si–Si bonds. *Journal of applied physics, 100*(5), 053515.

Vons, V. A., de Smet, L. C., Munao, D., Evirgen, A., Kelder, E. M., & Schmidt-Ott, A. (2011). Silicon nanoparticles produced by spark discharge. *Journal of Nanoparticle Research, 13*(10), 4867.

Wang, Z., Ley, L., & Cardona, M. (1982). Infrared spectroscopy of amorphous hydrogenated GaAs: Evidence for H bridges. *Physical Review B, 26*(6), 3249.

Wells, R. L., Pitt, C. G., McPhail, A. T., Purdy, A. P., Shafieezad, S., & Hallock, R. B. (1989). The use of tris (trimethylsilyl) arsine to prepare gallium arsenide and indium arsenide. *Chemistry of Materials, 1*(1), 4-6.

Chapter 4.

Long-time Consistent Nanoparticle Generation Utilizing Wire-in-Hole Type Spark Discharge Generator

4.1. Introduction

Spark discharge generation (Schwyn et al., 1988) is a simple, clean and reliable method for generating nanometer-sized particles among diverse gas-phase synthesis techniques. Particles synthesized via a spark discharge generator can be directly used for the enhancement of many electronic and catalytic properties, for example, to increase the efficiency of an organic display device (Sung et al, 2014), to improve the performance of catalysts (Messing et al., 2009), and to generate gold seed particles for nanowire growth (Messing et al., 2009). Furthermore, spark discharge generation can produce nanoparticles using diverse materials having varied properties, such as bimetallic and mixed metallic nanoparticles (Byeon et al., 2008), and nanocomposites (Kala et al., 2013). In addition, this technique has been utilized to generate various types of charged aerosols, which enables the positioning of particles at precise locations on a dielectric surface (Krinke et al., 2002) and the fabrication of nanostructures via controlled electric field (Kim et al., 2006; You et al., 2010; Lee et al., 2011; Jung et al., 2014).

Up until now, rod-to-rod type spark discharge generators (RR-SDG) have been widely studied, and the effects of the process parameters have been well understood (Horvath and Gangl, 2003; Roth et al., 2004; Tabrizi et al., 2009). However, particles generated by RR-SDG are prone to agglomeration at high number concentrations due to post-discharge diffusion charging in bipolar ion clouds (Bau et al., 2010). In an effort to prevent agglomeration of the particles,

various methods have been developed such as controlling the flow rate of the carrier gas (Schwyn et al., 1988; Tabrizi et al., 2009) or injecting unipolar charged air ions (Park et al, 2014).

Recently, a pin-to-plate type spark discharge generator (PP-SDG), having asymmetric electrodes consisting of a sharp pin and a plate with a hole, was introduced which generates less agglomerated sub-10 nm nanoparticles with high concentration than the RR-SDG at the same condition (Han et al., 2012). This is attributed to the much faster transport of as-generated particles in the PP-SDG. Furthermore, the PP-SDG can be easily scaled up by employing multiple pin electrodes and corresponding exit holes in the flat-plate ground electrode (Ha et al, 2014). Despite such merits, the PP-SDG generated the particle size and the number concentration which evolve over time due to changes in the electrode geometry, such as gradual increases in the radius of curvature of the pin and in the distance between the pin and the plate as the pin electrode gets eroded with time. These factors cause changes in spark discharge properties. In this study, to maintain the size distribution of produced nanoparticles over a long time while producing small and unagglomerated nanoparticles with high concentration, we designed a new type of spark discharge generator comprising a metal wire as a positive electrode and a grounded plate with a hole. The wire was placed in the center of an exit hole in the plate. Using this newly designed wire-in-hole type spark discharge generator (WH-SDG), we measured geometric mean diameter

(GMD) and particle number concentration for twelve hours at various carrier gas flowrates. In addition, the versatility and controllability of the new design was demonstrated with different kinds of metal such as Cu and Pd.

4.2. Experimental Methods

The experimental setup consists of a spark discharge generator, an electrostatic precipitator and a scanning mobility particle sizer (SMPS) system with an aerosol neutralizer, which is a commonly used particle measurement setup, as depicted in Figure 4.1(a) (Byeon et al., 2008; Tabrizi et al., 2009; Han et al., 2012). The spark discharge generator was made up of a cylindrical chamber, two electrodes, electrode holders and an inlet and an outlet for carrier gas flow. The inner diameter of the chamber is 40 mm and the length is 30 mm. The electrode holders were precisely machined and assembled at the center of the chamber. Alignment of the geometric condition of electrodes was controlled by putting the ground electrode on the 2-axis micro stage. Silver, copper and palladium (99.99% purity) were used as materials for electrodes. Nitrogen (99.999% purity) was used as the carrier gas, and the flow rate was set at 2 lpm. The size distribution of the generated particles was measured with a differential mobility analyzer (DMA, TSI 3085), a condensation nuclei counter (CNC, TSI 3776) and an Am-241 aerosol neutralizer (Grimm #5.521). The generated particles were transported to the DMA and the CNC, passing through an aerosol neutralizer. The flowrates of sheath and aerosol gas of DMA were set at 15 lpm and 1.5 lpm, respectively. The positively charged nanoparticles were collected on a carbon film-coated copper grid using electrostatic precipitator for 3 minutes. and imaged using high resolution-transmission electron microscope (HR-TEM,

JEOL ARM 200F).

The circuit that provides electric power to the spark discharge generator is shown in Figure 4.1(b). Similar circuits have been widely used by other researchers to regulate the spark discharge characteristics (Schwyn et al., 1988; Horvath and Gangl, 2003; Tabrizi et al., 2009; Han et al., 2012; Pfeiffer et al., 2014). It consists of a high voltage power supply, an external capacitor (C_{ext}) and a resistor (R_c). Charging time of the external capacitor (C_{ext}) can be chosen by selecting the resistance value of the external resistor (R_c) which is depicted in figure 4.1(b). To generate nanoparticles which have desirable particle size distribution, the value of the external capacitor and the external resistor was determined. The high-voltage DC power supply (FuG HCP35-6500) with a maximum voltage of 6.5 kV was connected to one end of the resistor. High voltage power supply output (V_{input}) was set at 6 kV to charge the external capacitor. The external capacitor which is much larger than the intrinsic capacitance between the two electrodes in SDG was connected in parallel to the electrode. Discharge voltage and spark frequency were measured with an oscilloscope (Agilent DSO-X 3014A) and a high voltage probe (Tektronix P6015A).

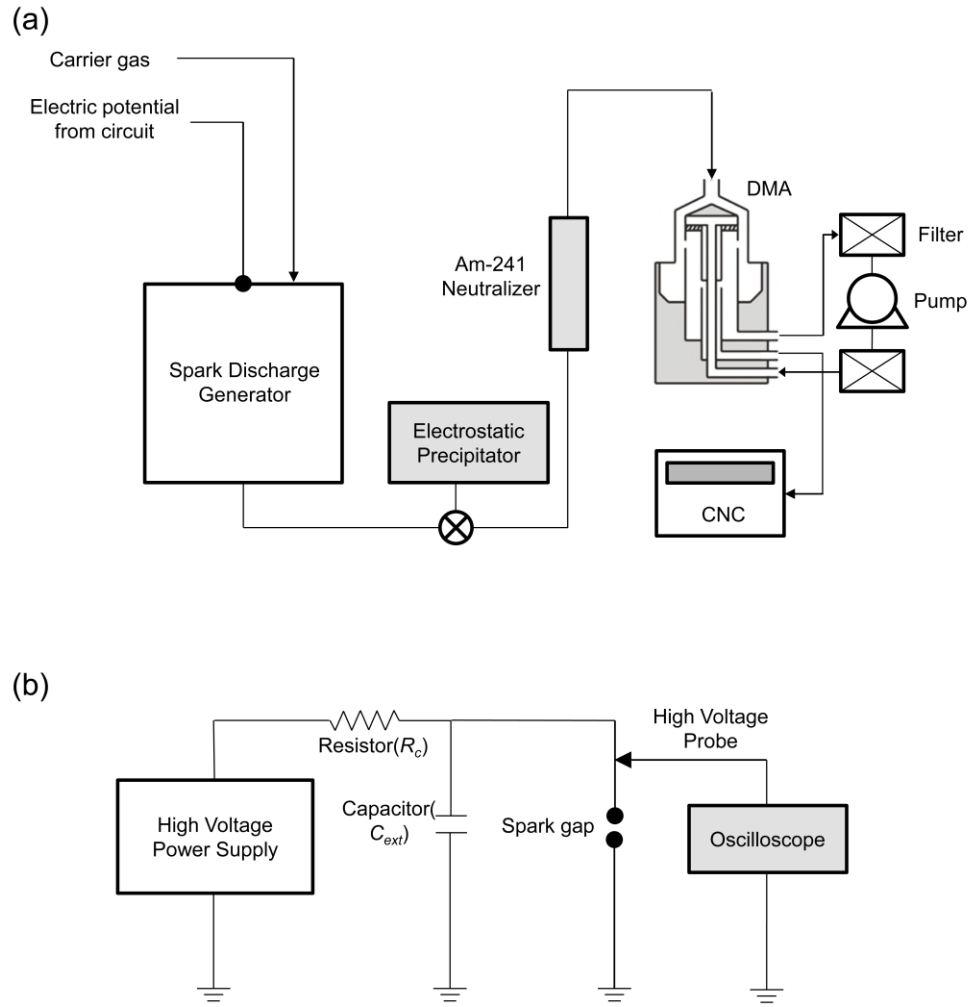

Figure 4.1. Spark discharge system and experimental setup (a) experimental schematic of the particle generation and measurement system. (b) Schematic of the electric circuit in a spark discharge generator.

We investigated the characteristics of four different electrode configurations as depicted in Figure 4.2: rod-to-rod, pin-to-plate, wire-in-hole and wire-to-plate configuration. For the rod-to-rod configuration, the diameter of cylindrical rod electrodes was 7 mm and the gap between the two electrodes was 0.75 mm. In the case of the pin-to-plate configuration, a pin electrode that had 7 mm diameter was machined to have a sharp tip with a radius of curvature of approximately 0.12 mm. The diameter of wire electrodes used in the wire-in-hole and wire-to-plate configuration was 0.5 mm and the wire electrodes were placed precisely in the center of the hole. The grounded electrode plate for the pin-to-plate, wire-in-hole and wire-to-plate configuration had the exit hole with a diameter of 2 mm in the center of the grounded plate electrode. The initial gap between the wire and the grounded plate was 0.75 mm for both the pin-to-plate type and the rod-to-rod type SDG.

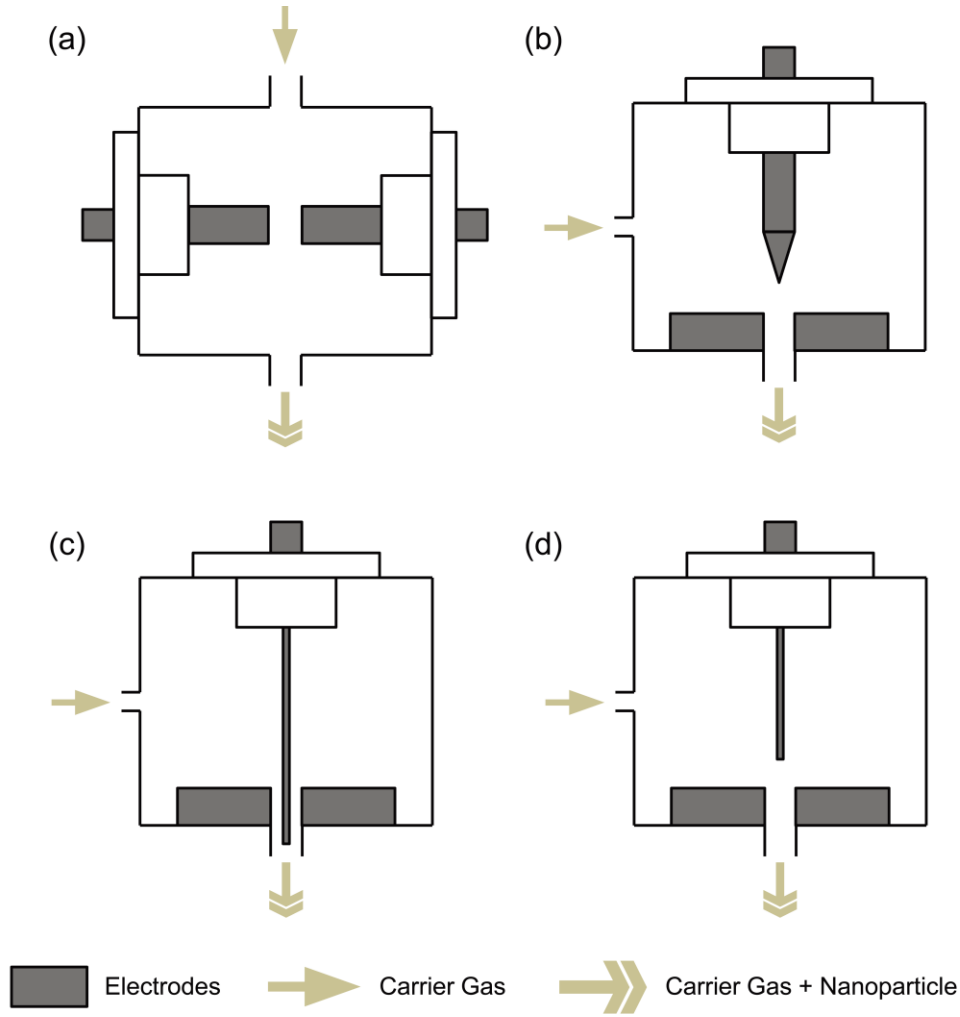

Figure 4.2. Four different types of spark discharge generator. (a) Rod-to-rod type electrode configuration. (b) Pin-to-plate type electrode configuration. (c) Wire-in-hole type electrode configuration. (d) Wire-to-plate electrode configuration.

4.3. Results and Discussion

The particle generation and size measurement were carried out continuously for 12 hours for the RR-SDG and the PP-SDG. Figure 4.3 shows the morphologies and size distribution of Ag nanoparticles generated by the rod-to-rod and pin-to-plate type generator. Each sub-figure shows a TEM image sampled before (Fig 4.3(a), 4.3(d)) and after tests which were conducted for 12 hours (Fig 4.3(b), 4.3(e)). SMPS measurements were also carried out every 3 hours to obtain the size distribution data (Figure 4.3(c) and 4.3(f)). RR-SDG generated Ag particles with a wider size distribution than PP-SDG producing less agglomerated particles than RR-SDG. The geometric standard deviation (σ_g) and the geometric mean diameter (d_g) of the RR-SDG were 1.46 and 7.21 nm, respectively. On the contrary, the Ag nanoparticles generated by the pin-to-plate configuration showed a narrower size distribution with lower geometric standard deviation ($\sigma_g = 1.36$) than that of the RR-SDG. In the case of the PP-SDG, the size distribution of the particles became narrower over 12 hours. The diameter (d_g) which was initially 7.32 nm declined gradually to 4.91 nm after 12 hours. The total number concentration of generated particles also decreased from 1.12×10^8 #/cm^3 to 5.70×10^7 #/cm^3, as shown in Figure 4.3(f). For the rod-to-rod type generator, the size distribution did not change over time (with a minute difference of 0.21 nm in diameter produced for 12 hours) as shown in Figure 4.3(c).

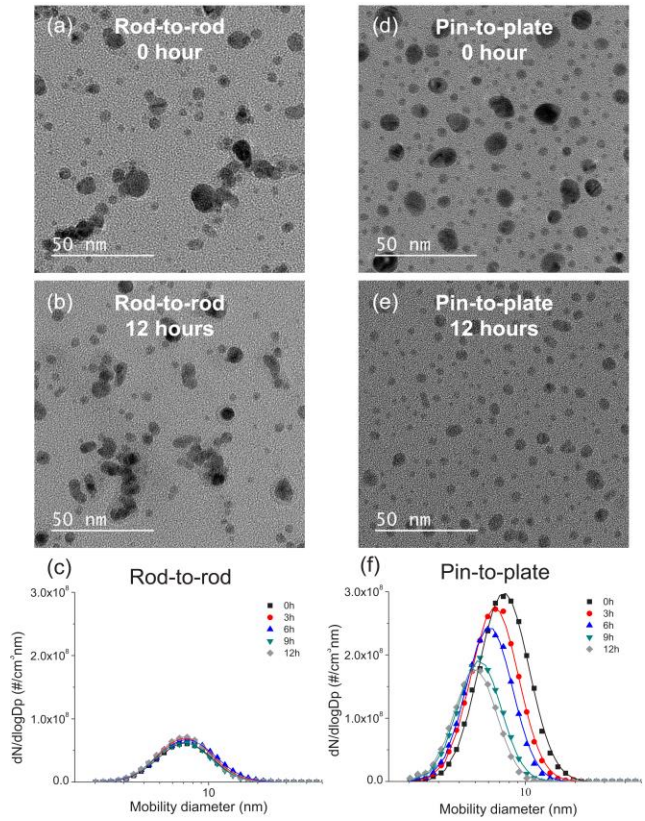

Figure 4.3. Ag nanoparticles generated via two different types of spark discharge generator. (a) A TEM image of nanoparticles for rod-to-rod type SDG at the beginning of the experiment. (b) A TEM image of nanoparticles for rod-to-rod type SDG after 12 hours from the beginning. (c) Size distribution of rod-to-rod type SDG measured every 3 hours. (d) A TEM image of nanoparticles for pin-to-plate type SDG at the beginning of the experiment. (e) A TEM image of nanoparticles for pin-to-plate type SDG after 12 hours from the beginning. (f) Size distributions of nanoparticles produced by the pin-to-plate type SDG measured every 3 hours.

To investigate why the size distribution of PP-SDG generated particles gradually change over time, the tip shape of the pin electrode and spark characteristics were measured. During the spark discharge process, the tip of the pin electrode was eroded, consequently increasing both the radius of curvature of the pin electrode and the distance between the pin and the plate electrode. Figure 4.4(a) ~ 4.4(e) show the changes in the shape of the pin electrode. The sharp pin electrode with 0.12 mm radius of curvature (Figure 4.4(a)) was eroded, thus the gap distance increased and the shape of the tip became blunt. The increase in the radius of curvature of the pin electrode and in the gap distance between the two electrodes affects the discharge characteristics such as discharge voltage and spark frequency. Due to these factors, increased electric field is required to produce sparks between the pin and the plate electrode, so consequently the discharge voltage gets increased. The electric potential of the electrode for RC circuit is defined as $V_{electrode}(t) = V_{input}(1-exp(^{-t}/_{RC}))$, where V_{input} is the output voltage of the power supply. As the resistance and the capacitance of the circuit are the same, increased discharge voltage requires more time for spark formation, which leads to a reduction in the spark discharge frequency. Figure 4.4(f) shows that the measured discharge voltage ($V_{discharge}$) increased from 3 kV at 0 hour to 4.2 kV after 12 hours and the spark frequency decreased from 101 Hz to 55.4 Hz during the time. Single spark discharge energy which is expressed as $E_{spark} = (^1/_2)C_{ext}V_{discharge}^2$, where $V_{discharge}$ is the voltage required to cause spark

discharge, increased due to larger $V_{discharge}$. The spark discharge power is expressed as the product of the spark discharge energy and its frequency. The spark discharge power remained almost constant during the experiment. This means that the spark energy is dispersed in larger volumes as the gap between the two electrodes increases, and less energy is used for the evaporation of the electrodes. The decreased concentration of vaporized metal atoms causes the reduction in particle number concentration. In conclusion, tip erosion and gap distance increase can explain why the PP-SDG produces smaller particles as time passes whereas the RR-SDG produced particles with a constant size distribution regardless of the elapsed time.

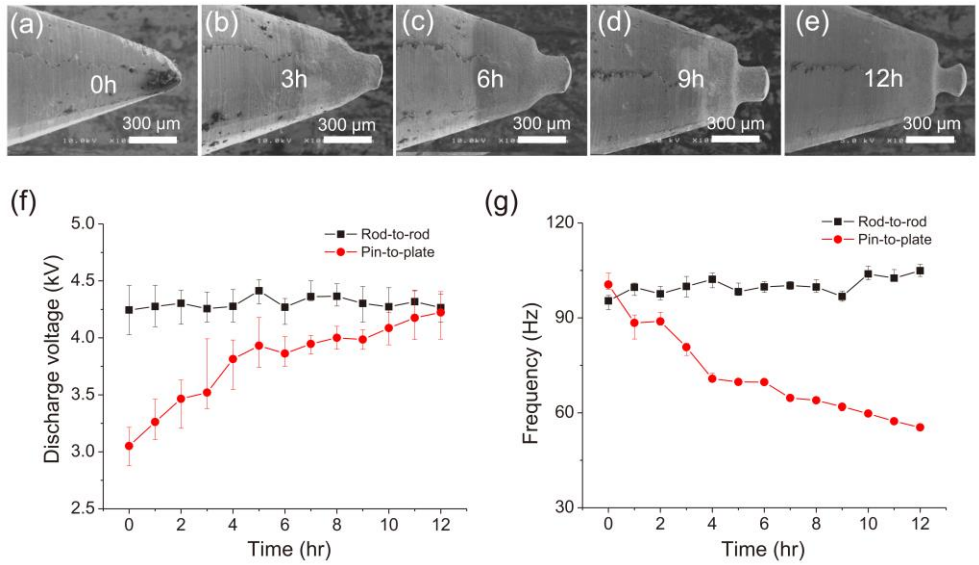

Figure 4.4. (a) ~ (e) Morphological changes in the tip of the pin electrode in a pin-to-plate type SDG. Changes in (f) spark discharge voltage and (g) frequency versus time for both SDGs.

To maintain the fast local carrier gas velocity of the PP-SDG and to suppress the shape change of the positive electrode at the same time, we designed a new type of spark discharge chamber, called the wire-in-hole type spark discharge generator (WH-SDG) which exploits a metal wire located in the center of an exit hole in the plate. The size distribution and the morphology of particles generated by WH-SDG are depicted in Figure 4.5. The size distribution did not change significantly for 12 hours, with d_g of 5.5 nm and σ_g of 1.35 maintaining the high number concentration of 7.34×10^7 #/cm^3 as measured by an SMPS (Figure 4.5(c)). The TEM images of the particles after 0 hour and 12 hours elapsed confirm that the particle size distribution did not change. The particle size distributions from the TEM image were well consistent with that from SMPS measurements. The geometrical configuration of the WH-SDG can effectively restrain the change in the gap distance, and the changes in the electrode geometry were relatively insignificant. Thus, it was demonstrated that the WH-SDG can generate the unagglomerated nanoparticles with high number concentration consistently for several hours.

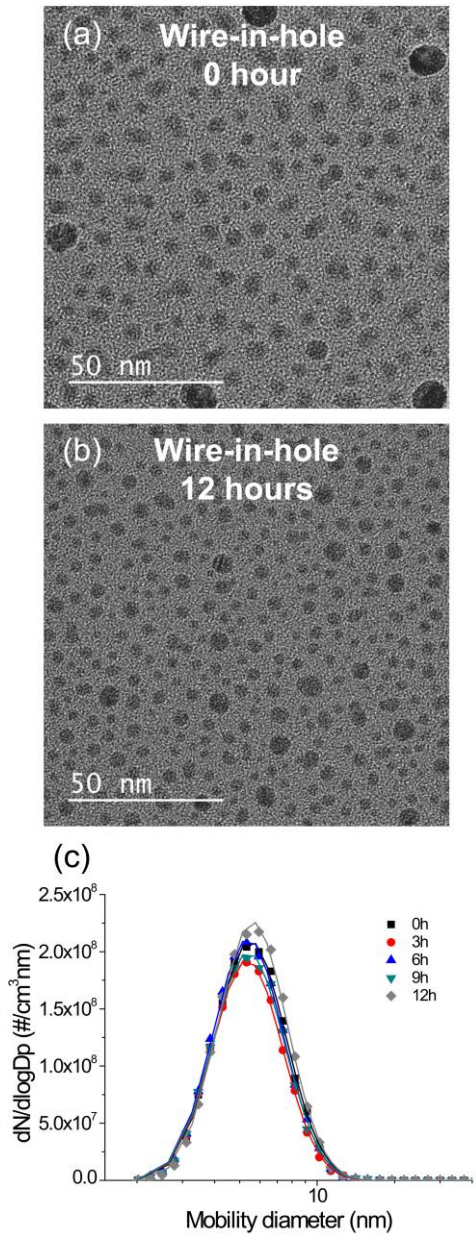

Figure 4.5. Ag nanoparticles produced via wire-in-hole type SDG. (a) A TEM image of nanoparticles at the beginning. (b) A TEM image of nanoparticles after 12 hours from the beginning. (c) Size distributions of produced nanoparticles measured every 3 hours.

Figure 4.6(a) ~ 4.6(e) show the images of the wire electrode over time. The wire electrode was worn in the radial direction in the region less than 100 μm from the tip. The spark discharge occurred at various points around the gap of the wire and the grounded plate, which resulted in evenly distributed sparks around the whole surface of the wire electrode. Since the surface area of the electrode subject to erosion is larger than that of the PP-SDG, the WH-SDG can maintain consistent spark discharge characteristics for a longer time. The discharge voltage and the spark frequency of the WH-SDG were measured with an oscilloscope. The discharge voltage ($V_{discharge}$) stayed at approximately 3.28 kV and the spark frequency was stayed at approximately 90.8 Hz for 12 hours with small fluctuations (±0.13 kV and ±3.7 Hz respectively), as shown in Fig 6(f) and 6(g).

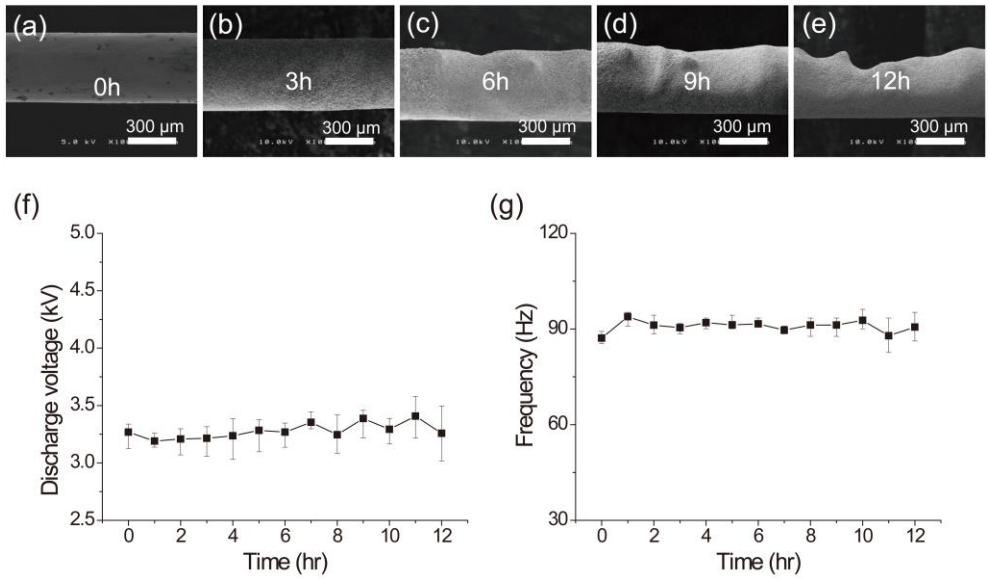

Figure 4.6. (a) ~ (e) Morphological changes in the wire electrode in wire-in-hole type SDG. Changes in (f) spark discharge voltage and (g) frequency versus time for WH-SDG.

The particle size distributions obtained from various types of the spark discharge generators for 12 hours are plotted in Figure 4.7. In addition to the PP-SDG and the WH-SDG, the wire-to-plate spark discharge generator (WP-SDG, see Figure 4.2(d)) was tested in the experiment to exclude the effects of tip shape changes, and determine the influence of the gap distance changes more clearly. From Figure 4.7(a), the geometric mean diameter of the WH-SDG was maintained at 5.5 nm for 12 hours, but in the case of the PP-SDG and the WP-SDG, the d_g were decreased from 7.32 to 4.90 nm, and from 7.72 to 4.60 nm, respectively. There was a similar trend for the number concentration. The WH-SDG showed the high number concentration of 7.34 $\times$ 10^7 #/cm^3 steadily, while the number concentration of the PP-SDG and the WP-SDG decreased (Figure 4.7(b)). The total number concentration of the PP-SDG was initially 1.12 $\times$ 10^8 #/cm^3 and decreased to 5.70 $\times$ 10^7#/cm^3. In the case of the WP-SDG, the total number concentration also decreased from 1.30 $\times$ 10^8 #/cm^3 to 3.59 $\times$ 10^7 #/cm^3. This shows that the PP-SDG showed decreasing size distribution due to the change in both the tip shape and the gap distance. The increasing gap distance can reduce the particle size and quantity, which can be inferred from the case of the WP-SDG.

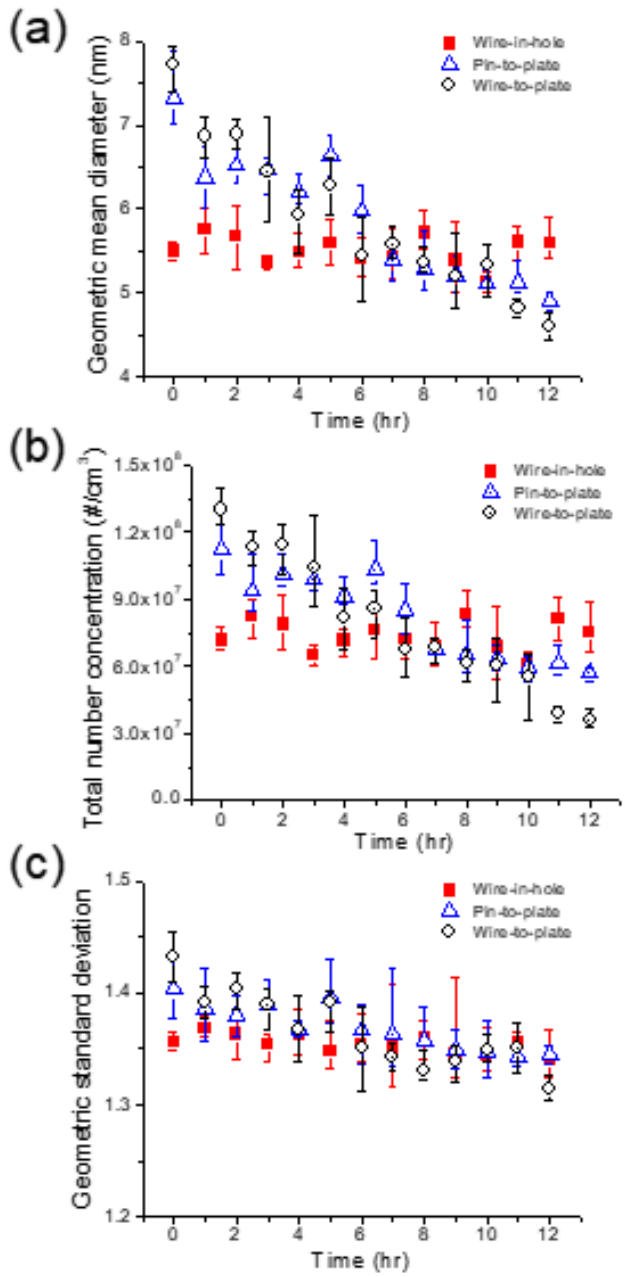

Figure 4.7. Characteristics of particles generated via WH-SDG, PP-SDG and WP-SDG versus time. (a) Geometric mean diameter. (b) Total number concentration. (c) Geometric standard deviation.

Further, in order to utilize the generated nanoparticles as building blocks for nanostructures, it is important to control the size of the generated particles. Thus, we conducted an additional experiment for controlling particle sizes with respect to gas flow rate. Since the increased gas flow rate enhances cooling and dilution rate (Lehtinen and Zachariah, 2002; Tabrizi et al., 2009), the size of the generated nanoparticles is sensitive to the flow rate of the carrier gas. Hence, we measured the size distribution with using different carrier gas flow rates of 1 lpm, 2 lpm and 4 lpm. The discharge voltage and spark frequency of all experiments were maintained during the particle generation. As shown in Figure 4.8, the particle diameter became smaller as the gas flow rate increased. The average mobility diameter is 6.50 nm, 5.51 nm and 5.15 nm for 1 lpm, 2 lpm and 4 lpm, respectively. For the flow rate of 1 lpm, the particle diameter was obviously larger than that of the case for 2 lpm due to the difference in residence time. But the difference in diameter between 2 lpm and 4 lpm cases was somewhat smaller than that between 1 lpm and 2 lpm cases. The geometric standard deviation of size distribution for 1 lpm condition was 1.38 and was slightly higher than the size distribution of 2 lpm condition (σ_g = 1.35) as shown in Figure 4.8(c). The difference of σ_g between 2 lpm and 4 lpm cases was much smaller than that between 1 lpm and 2 lpm cases. These results imply that lower flow rate can make larger particles and may cause agglomeration but the effect is insignificant. (Tabrizi et al., 2009) If the flow rate increases, the diameters of the generated particles

become smaller because higher transport velocity in particle growth regions can lower the probability of aggregation (Han et al., 2012).

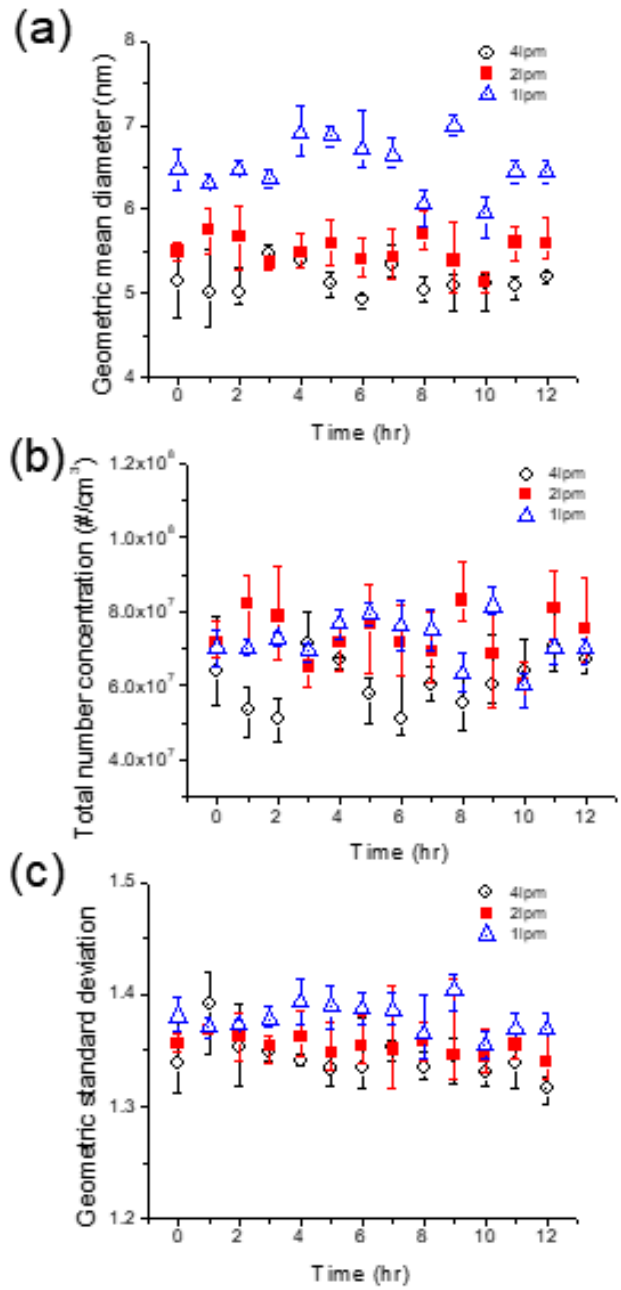

Figure 4.8. Size distributions of generated nanoparticles with different gas flow rate. (a) Geometric mean diameter (b) Total number concentration (c) Geometric standard deviation.

To show the versatility of the system, other materials such as copper and palladium were used in the WH-SDG as electrodes and the performance evaluation was carried out (Figure 4.9). The experimental conditions were set for generating nanoparticles of 5 nm in diameter. In the case of silver and copper, the electric circuit was comprised of a 5 MΩ charging resistor and a 2nF external capacitor. For palladium nanoparticles, the resistance and the capacitance of the circuit were 20 MΩ and 1 nF, respectively. The gas flow rate for Pd particle generation was set at 3 lpm to avoid agglomeration. As shown in Figure 4.9, the size distributions were maintained with little fluctuation. The average geometric standard deviations were 1.35, 1.32 and 1.31 for silver, copper and palladium, respectively.

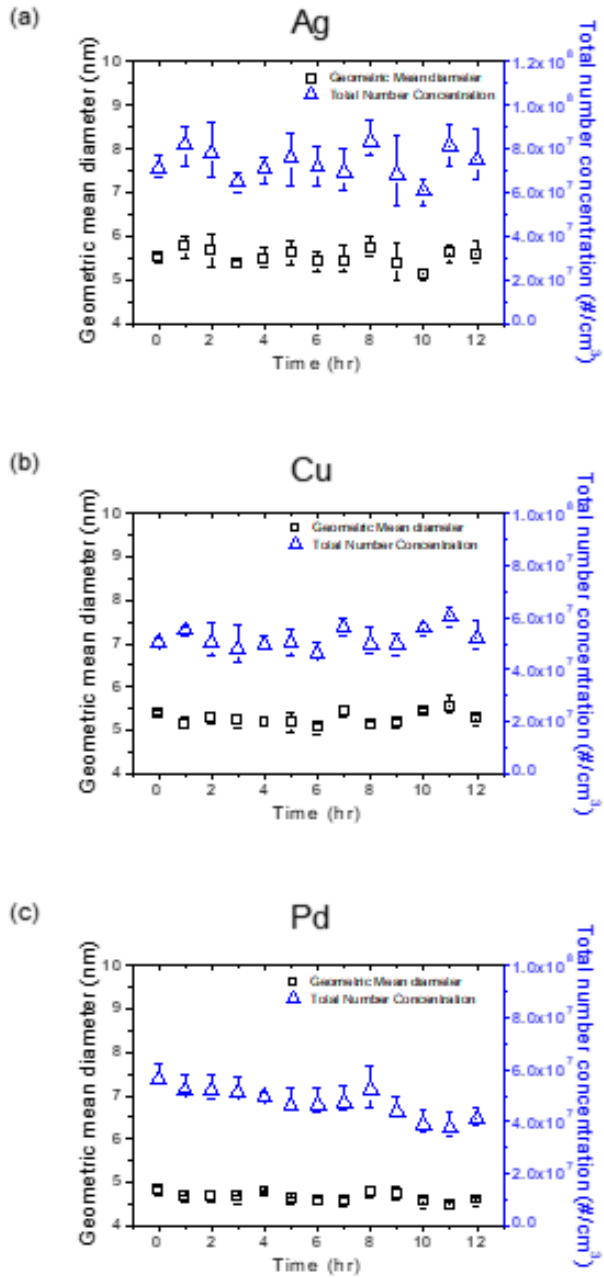

Figure 4.9. Geometric mean diameters and total number concentrations of various metal nanoparticles generated by WH-SDG over 12 hours. (a) Silver (b) Copper (c) Palladium

4.4. Conclusion

In this study, we developed and evaluated a new type of SDG, in which a metal wire was used as an electrode and the wire electrode was designed to be located in the center of the hole on the grounded plate electrode. Using this wire-in-hole type SDG, it was possible not only to generate unagglomerated nanoparticles with high concentration, but also to show more consistent size distributions for longer operations than the previous pin-to-plate type SDG. The change in the particle size distribution of the PP-SDG over time was found to be due to the changes in the geometry of the pin electrode caused by repetitive spark discharges. The transformed electrode geometry led to the change in spark discharge characteristics such as spark discharge voltage and frequency which could directly influence the generation of nanoparticles. On the other hand, the WH-SDG could effectively suppress the change of gap distance and the shape of the electrode and, hence, maintain its spark discharge properties for a longer time.

Further, to control the diameter of the generated nanoparticles, we carried out experiments varying the flow rates of the carrier gas. As expected, the increasing flow rates from 1 lpm to 4 lpm could produce smaller diameters of nanoparticles. In addition, WH-SDG was able to produce and maintain unagglomerated metal nanoparticles such as Ag, Cu and Pd for a long time.

Thus, the WH-SDG has a novel advantage over other electrode configurations as it can produce small and unagglomerated nanoparticles

consistently for several hours. This capability will be especially advantageous for utilization of produced nanoparticles as building blocks to fabricate nanostructures with complex morphologies.

4.5. References

Bau, S., Witschger, O., Gensdarmes, F., Thomas, D., Borra, J. P. (2010). Electrical properties of airborne nanoparticles produced by a commercial spark-discharge generator. J. Nanoparticle Res. 12:1989-1995.

Borra, J. P., Goldman, A., Goldman, M., Boulaud, D. (1998). Electrical discharge regimes and aerosol production in point-to-plane dc high-pressure cold plasmas: Aerosol production by electrical discharges. J. Aerosol Sci. 29:661-674.

Borra, J. P., Jidenko, N., Dutouquet, C., Aguerre, O., Hou, J., Weber, A. (2011). Nano-droplet ejection and nucleation of materials submitted to non-thermal plasma filaments. European Physical Journal-Applied Physics 56:24019.

Byeon, J. H., Park, J. H., Hwang, J. H. (2008). Spark generation of monometallic and bimetallic aerosol nanoparticles. J. Aerosol Sci. 39:888-896.

Evans, D. E., Harrison, R. M., Ayres, J. G. (2003). The generation and characterisation of elemental carbon aerosols for human challenge studies. J. Aerosol Sci. 34:1023-1041.

Ha, K., Choi, H., Jung, K., Han, K., Lee, J.-K., Ahn, K., Choi, M. (2014). Large-area assembly of three-dimensional nanoparticle structures via ion assisted aerosol lithography with a multi-pin spark discharge

generator. Nanotechnology 25:225302.

Han, K., Kim, W., Yu, J., Lee, J., Lee, H., Woo, C. G., Choi, M. (2012). A study of pin-to-plate type spark discharge generator for producing unagglomerated nanoaerosols. J. Aerosol Sci. 52:80-88.

Horvath, H. and Gangl, M. (2003). A low-voltage spark generator for production of carbon particles. J. Aerosol Sci. 34:1581-1588.

Jung, K., Hahn, J., In, S., Bae, Y., Lee, H., Pikhitsa, P. V., Ahn, K., Ha, K., Lee, J. K., Park, N., Choi, M. (2014). Hotspot-Engineered 3D Multipetal Flower Assemblies for Surface-Enhanced Raman Spectroscopy. Adv. Mater. 26:5924-5929.

Kala, S., Theissmann, R., Kruis, F. E. (2013). Generation of AuGe nanocomposites by co-sparking technique and their photoluminescence properties. Journal of Nanoparticle Research 15:1963-1974.

Kim, H., Kim, J., Yang, H.J., Suh, J., Kim, T., Han, B.W., Kim, S., Kim, D.S., Pikhitsa, P.V., & Choi, M. (2006). Parallel patterning of nanoparticles via electrodynamic focusing of charged aerosols. Nature Nanotechnology 1:117-121.

Krinke, T. J., Fissan, H., Deppert, K., Magnusson, M. H., Samuelson, L. (2001). Positioning of nanometer-sized particles on flat surfaces by direct deposition from the gas phase. Applied Physics Letters 78:3708-3710.

Lee, H., You, S., Pikhitsa, P. V., Kim, J., Kwon, S., Woo, C. G., Choi, M. (2011). Three-Dimensional Assembly of Nanoparticles from Charged Aerosols. Nano Letters 11:119-124.

Lehtinen, K. E. J. and Zachariah, M. R. (2002). Energy accumulation in nanoparticle collision and coalescence processes. J. Aerosol Sci. 33:357-368.

Messing, M. E., Dick, K. A., Wallenberg, L. R., Deppert, K. (2009). Generation of size-selected gold nanoparticles by spark discharge - for growth of epitaxial nanowires. Gold Bulletin 42:20-26.

Meuller, B. O., Messing, M. E., Engberg, D. L. J., Jansson, A. M., Johansson, L. I. M., Norlen, S. M., Tureson, N., Deppert, K. (2012). Review of Spark Discharge Generators for Production of Nanoparticle Aerosols. Aerosol Sci. Technol. 46:1256-1270.

Park, K. T., Farid, M. M., Hwang, J. (2014). Anti-agglomeration of spark discharge-generated aerosols via unipolar air ions. J. Aerosol Sci. 67:144-156.

Pfeiffer, T. V., Feng, J., Schmidt-Ott, A. (2014). New developments in spark production of nanoparticles. Advanced Powder Technology 25:56-70.

Roth, C., Ferron, G. A., Karg, E., Lentner, B., Schumann, G., Takenaka, S., Heyder, J. (2004). Generation of ultrafine particles by spark discharging. Aerosol Sci. Technol. 38:228-235.

Schwyn, S., Garwin, E., Schmidtott, A. (1988). Aerosol Generation by Spark

Discharge. J. Aerosol Sci. 19:639-642.

Sung, H., Lee, J., Han, K., Lee, J. K., Sung, J., Kim, D., Choi, M., Kim, C. (2014). Controlled positioning of metal nanoparticles in an organic light-emitting device for enhanced quantum efficiency. Organic Electronics 15:491-499.

Tabrizi, N. S., Ullmann, M., Vons, V. A., Lafont, U., Schmidt-Ott, A. (2009). Generation of nanoparticles by spark discharge. J. Nanoparticle Res. 11:315-332.

Watters, R. L., Devoe, J. R., Shen, F. H., Small, J. A., Marinenko, R. B. (1989). Characteristics of Aerosols Produced by the Spark Discharge. Analytical Chemistry 61:1826-1833.

You, S., Han, K., Kim, H., Lee, H., Woo, C. G., Jeong, C., Nam, W., Choi, M. (2010). High-Resolution, Parallel Patterning of Nanoparticles via an Ion-Induced Focusing Mask. Small 6:2146-2152.

Chapter 5.

High Throughput Nanoparticle Generation Utilizing High Frequency Spark Discharges via Rapid Spark Plasma Removal

5.1. Introduction

Spark discharge generation (Schwyn et al. 1988) is a simple, clean and energy efficient method for producing nanoparticles in gas phase media (Borra 2006; Meuller et al. 2012; Park et al. 2014; Tabrizi et al. 2009), and the nanoparticles generated by this method have been utilized in various applications for their unique optical, electrical and catalytic properties. For example, gold nanoparticles produced by the spark discharge method were employed in organic light emitting diode devices to enhance their quantum efficiency (Sung et al. 2014) and used as seeds for nanowire growth (Messing et al. 2009). In addition, charged nanoparticles produced from spark discharges can be directed via electrostatic field and assembled into complex three dimensional nanostructures which can be utilized for various applications; for example, in surface enhanced Raman spectroscopy (Jung et al. 2014; Lee et al. 2010), gas sensing (Lee et al. 2010) and photovoltaics (Ha et al. 2016; Jang et al. 2016; Kim et al. 2015).

To integrate spark discharge generated nanoparticles into industrial applications, the ability to scale up the manufacturing process in a uniform and stable manner is essential. There are many ways to increase the production rate of a single set of electrodes, one of which is to increase the spark frequency. Each spark discharge can be thought of as a unit event that generates a certain amount of nanoparticles, and the production rate is expected to scale linearly with the spark frequency. In reality, this is not the

case as at high frequency regime above 1 kHz, premature spark discharges occur intermittently, resulting in a production rate that is lower than expected (Pfeiffer et al. 2014). Of note, a recent review article by Pfeiffer et al. (2014) has demonstrated spark stability up to 20 kHz by adding fast switching electronic components to the conventional circuit to prevent premature spark discharges and to regulate the spark duration.

In this study, we sought to stabilize the spark discharge process at high frequencies by first determining the factors which affect the spark stability. We hypothesized that the residual spark plasma is the cause of premature spark discharges, and hence developed a wire-to-plate electrode configuration (Maisser et al. 2015) which has increased local carrier gas flow velocity and electric field intensity around the spark zone, both of which are expected to contribute to fast removal of spark plasma generated by the preceding spark event. The maximum stable spark frequency and spark duration of wire-to-plate electrodes were compared against those of rod-to-rod and wire-to-rod electrodes and the effect of the electric field intensity and gas velocity were confirmed separately. Then, the nanoparticle production rates were quantified for high frequency operations to confirm that the production rates scale up as expected. Lastly, changes in size distributions depending on the operation frequency are noted and its implications are discussed.

5.2. Experimental Methods

The experimental setup shown in Figure 5.1(a) was used to generate nanoparticles and measure the size distribution of the produced nanoparticles as well as to measure the voltage and current at the electrodes during the process.

The 'conventional' circuit was used to control the spark discharge (Chae et al. 2015; Han et al. 2012), comprising of a high voltage power source (HVPS, FuG HCP 350-12500), a resistor (200 or 400 kΩ) and a capacitor (1, 2 or 3 nF). The spark frequency was controlled by varying the voltage input from the HVPS and the resistance of the circuit, while other parameters (discharge voltage, mass flow rate of carrier gas and capacitance of the circuit) remained unchanged. An oscilloscope (Agilent DSO-X 3014 A) equipped with a high voltage probe (Tektronix P6015A) and a current probe (Agilent 1147A) was connected to the anode for voltage and current measurements.

The spark discharger was constructed using a custom cylindrical chamber (122 cm^3 volume, 50 mm inner diameter, 62 mm in height). Three different electrode configurations were used in this study: rod-to-rod (Figure 5.1(b)), wire-to-rod (Figure 5.1(c)) and wire-to-plate (Figure 5.1(d)). Copper rods (diameter, d = 7 mm) and wires (d = 1 mm) were used as electrodes for rod-to-rod and wire-to-rod configurations, and were installed horizontally and coaxially within the spark discharge chamber. For the wire-to-plate type electrode configuration, a copper wire (d = 1mm) electrode was installed

vertically on a holder and aligned to the central axis of the chamber. Then, a copper ground plate (which also serves as the cathode in this configuration) with a 0.5 mm diameter hole was mounted underneath the wire such that the hole is coaxially aligned with the wire electrode.

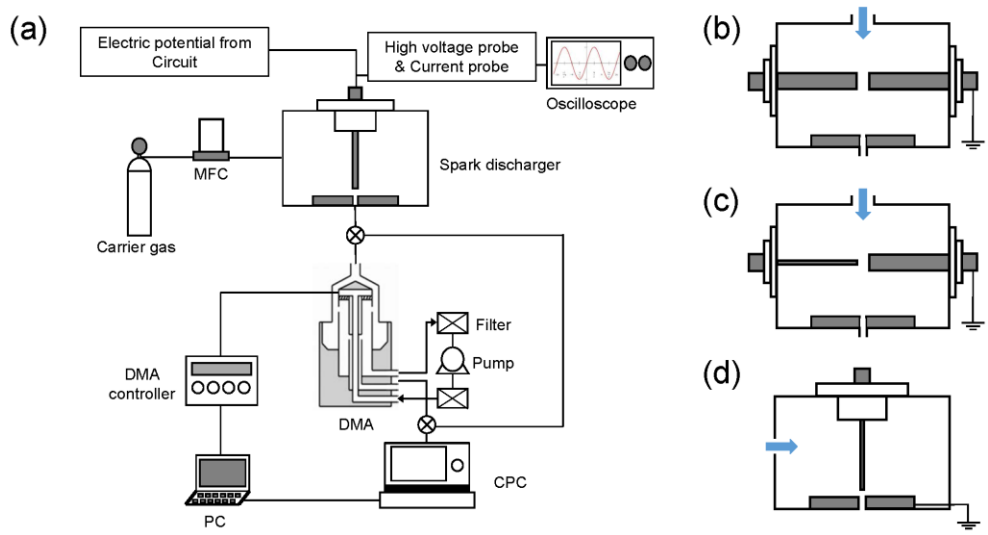

Figure 5.1. Schematics of (a) experimental setup (showing wire-to-plate electrode configuration as an example), and three different electrode configurations (b) rod-to-rod, (c) rod-to-plate and (d) wire-to-plate. Blue arrows in (b) – (d) indicate carrier gas inflow.

For all experiments, nitrogen (99.999 % purity) was used as the carrier gas, and its flow rate was controlled using a mass flow controller. The gas flow was directed such that it enters through the chamber inlet and exits through the hole (d = 0.5 mm) in the copper ground plate (In the rod-to-rod and wire-to-rod cases, the plate was still mounted to the chamber to keep the flow conditions the same as the wire-to-plate case.). The anode (wire electrode in the wire-to-rod configuration) was connected to the spark control circuit, and the cathode was connected to the ground. The gap between the electrodes was adjusted to set the discharge voltage at 2.2 kV.

The particle size distribution measurement system consists of a differential mobility analyzer (DMA, TSI 3085), a DMA controller (TSI 3776), and a condensation particle counter (CPC, TSI 3776). The DMA and CPC were used in conjunction to quantify the nanoparticles generated from the spark discharger in the range of 4-150 nm, and to obtain the particle size distribution.

5.3. Results and Discussion

For a spark discharge to occur, the voltage across the electrodes must exceed the breakdown voltage of the medium between them. Once the voltage exceeds the threshold value, dielectric breakdown of the medium occurs, and spark plasma is generated which completes the circuit and a current flows through the gap between the electrodes. Once the capacitor is discharged completely, the cycle starts again.

To determine the stability of the spark events, we monitored the voltage profiles across the spark electrodes using an oscilloscope and a high voltage probe. Figure 5.2(a) depicts an exemplary voltage profile of a stable spark discharge process with rod-to-rod electrodes where the spark discharge events occur at the desired voltage (~2.2 kV) consistently at a frequency of 1.1 kHz. When the spark frequency is increased to approximately 3.7 kHz, premature spark discharge events occur and spark discharge voltages as low as 600 V were observed (Figure 5.2(b)). The premature spark discharge occurs due to reduced breakdown voltage of the medium caused by residual space charge coming from the spark plasma that has not been completely removed (Pfeiffer et al. 2014). Therefore, to prevent premature spark discharges (or at least increase the onset frequency), it is necessary to restore the medium to its ‘normal’ state as quickly as possible before the next spark discharge event. The time needed for complete removal of the plasma may depend on a number of factors, such as the electrode geometry and configuration, carrier gas

velocity and the spark discharge voltage.

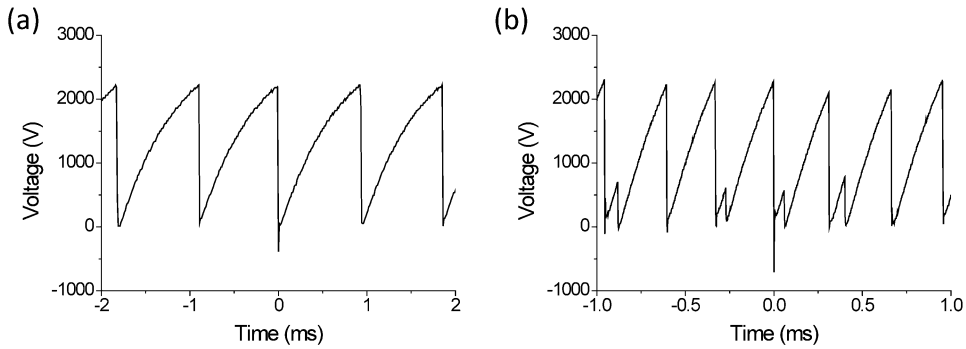

Figure 5.2. Voltage profiles from rod-to-rod electrode type spark discharger. (a) Frequency of 1.1 kHz. (b) Unstable state with discharge voltages below the desired breakdown voltage (2.2 kV)

Three electrode configurations were examined to identify the factors that affect the spark stability: rod-to-rod, wire-to-rod and wire-to-plate. Using 6.7 lpm of carrier gas flow, the maximum stable spark frequency was 1.1 kHz for rod-to-rod configuration, 2 kHz for wire-to-rod configuration, and 17.9 kHz for wire-to-plate configuration. This can be understood in terms of how fast the spark plasma is removed, and the medium returns to the 'normal' state. Indeed, at spark frequency of 1 kHz and carrier gas flow rate of 6.7 lpm, the voltage and current profiles of the three configurations show that the spark duration (defined as time for voltage/current oscillation to completely decay) is 5.45, 5.05, and 4.78 μs for rod-to-rod, wire-to-rod and wire-to-plate configurations respectively (Figure 5.3), where shorter duration is indicative of faster plasma removal. The differences in spark duration can be qualitatively explained by electrical repulsion from the high-intensity electric field and physical removal by the local carrier gas flow. The rod-to-rod and wire-to-rod configurations have similar local carrier gas velocity due to their geometric similarity, but the wire electrode in wire-to-plate configuration produces larger electric field intensity because of its thinner diameter, and hence the plasma is displaced faster by electrical repulsion. The wire-to-plate spark discharge generator was able to produce regular sparks at the highest frequency, which can be attributed to the fast local flow velocity near the spark region, in addition to the high electric field intensity arising from the wire electrode (Han et al. 2012).

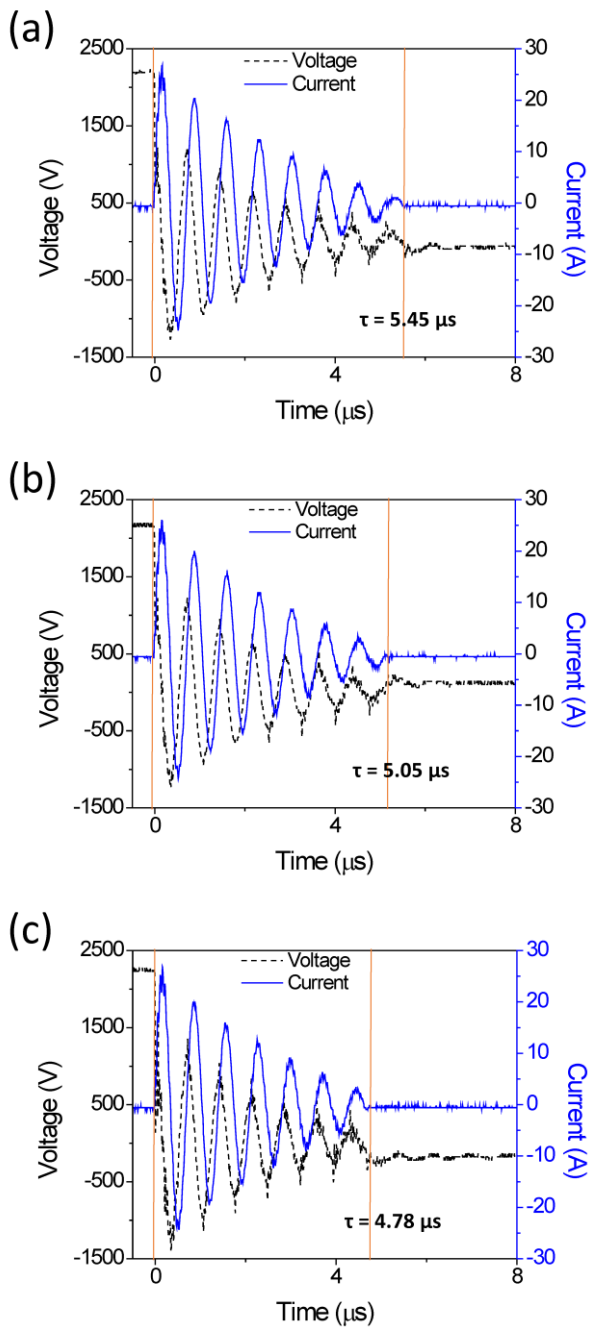

Figure 5.3. Current and voltage profiles during spark discharge events at 1 kHz spark frequency. (a) rod-to-rod, (b) wire-to-rod, and (c) wire-to-plate electrode configuration.

To validate the role of electric field intensity in spark discharge stabilization, we have measured the spark duration at different frequencies at a fixed carrier gas flow rate of 6.7 lpm (Figure 5.4). The average spark duration time decreased from 4.78 to 2.05 μs as the spark frequency increased from 1 kHz to 17.9 kHz. As faster restoration of the electrode potential leads to stronger electric field intensity, this result indicates that higher intensity electric fields help remove plasma faster, and thereby help stabilize the spark discharge process at high frequencies.

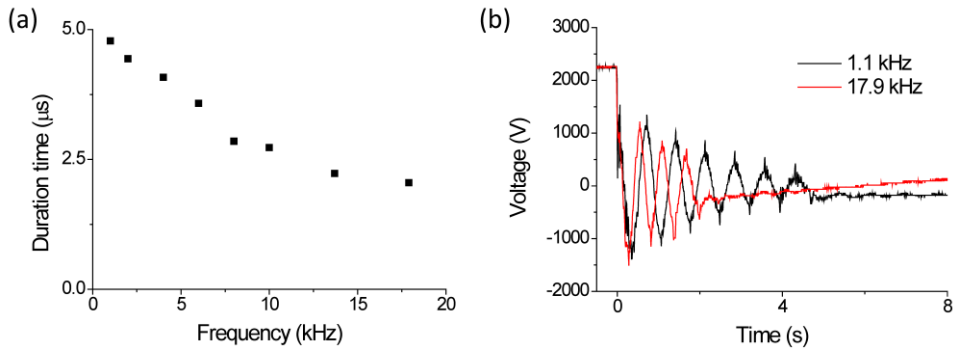

Figure 5.4. (a) Spark duration time of wire-to-plate electrode type spark discharger as spark frequency increases. (b) Voltage profiles during spark discharges events at 1.1 kHz and 17.9 kHz.

To confirm that the faster carrier gas flow helps stabilize spark events at higher frequencies, the voltage profiles for wire-to-plate electrodes set up for 14 kHz spark frequency using flow rates of 4.1 and 6.7 lpm were compared. At 4.1 lpm, premature spark discharges below the desired voltage of 2.2 kV occurred intermittently because the slow carrier gas flow was unable to eliminate the plasma between the electrodes (Figure 5.5(a)). At 6.7 lpm, the spark events occurred regularly, discharging at the desired voltage of 2.2 kV (Figure 5.5(b)). These results show that the faster carrier gas flow rate is indeed beneficial for high frequency operation of spark dischargers.

In addition to the stability of the spark events, we quantified the production rates of nanoparticles at different carrier gas flow rates. We chose the mass production rate to represent the production rate of nanoparticles, which can be approximated by the electrode ablation rate. The electrode ablation rate was measured by weighing the electrodes before and after spark discharge operations. The mass production rate should increase linearly with the spark frequency, as long as premature spark discharges do not occur. Indeed, it is seen that with 4.1 lpm of carrier gas flow, the mass production rate linearly increases with the frequency, up until ~14 kHz, after which premature spark discharges develop and the mass production rate drops off sharply. On the other hand, with 6.7 lpm flow, the mass production rate continues to increase linearly all the way up to 17.9 kHz (Figure 5.5(c)). The mass production rates measured within stable spark frequency range were consistent irrespective of

the carrier gas flow rate, which means that electrode ablation does not significantly depend on the carrier gas flow. The mass production rate also showed linear dependence on the circuit capacitance as expected (Figure 5.5(d)), and this shows that increasing the spark energy does not interfere with the spark stability. The electrode ablation efficiency was calculated to be 0.234×10^{-7} gJ^{-1} based on the total energy stored in the capacitor before discharge.

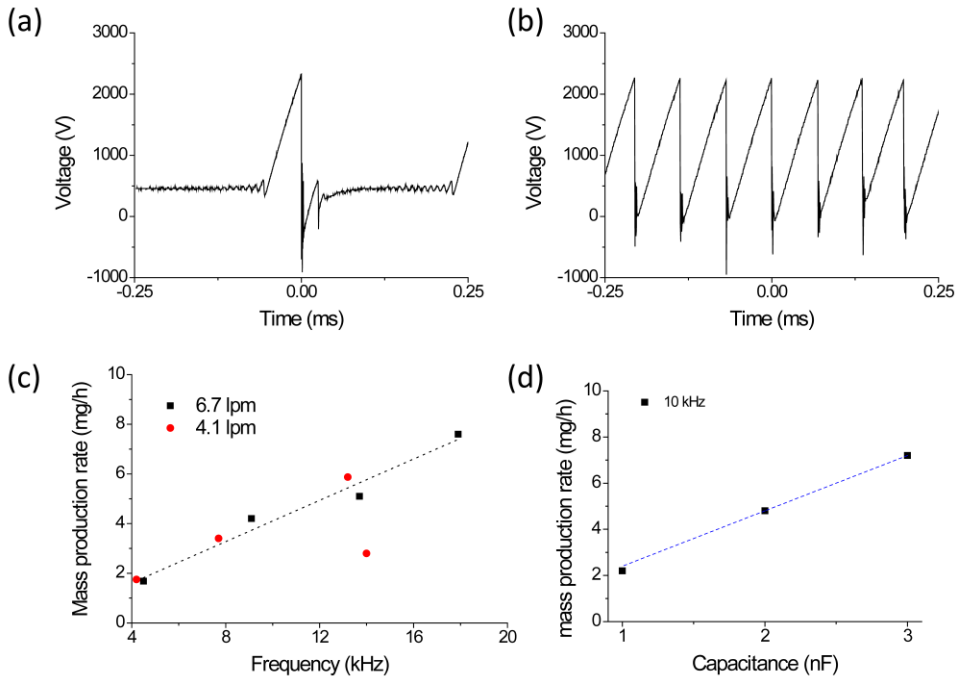

Figure 5.5. Voltage profiles from wire-to-plate electrode type spark discharger with frequency of 14 kHz with carrier gas flow rates of (a) 4.1 lpm and (b) 6.7 lpm. Mass production rate of nanoparticles scale linearly with (c) spark frequency, up to the maximum stable spark frequency, and (d) external capacitance, at spark frequency of 10 kHz and flow rate of 6.7 lpm.

Lastly, the particle size distributions were measured for spark frequencies of 4.5, 9.1 and 17.9 kHz to observe the effect of changing the spark frequency, while the carrier gas flow rate was kept at 6.7 lpm. Figure 6 (a), (b) and (c) show that the spark events are indeed stable for the tested frequencies of 4.5, 9.1 and 17.9 kHz, respectively. The geometric mean diameters were 11.0, 21.5 and 36.7 nm and the standard deviations were 1.40, 1.48 and 1.50, respectively. While the increase in spark frequency in a stable spark event leads to a linear increase in the mass production rate, the total number concentration and the mean particle diameter also increases with little changes to the standard deviation. This is expected as the flow conditions around the electrodes remain the same, while increased spark frequency would vaporize more material in a given time, increasing the concentration of primary particles that later agglomerate leading to larger mean particle diameters (Tabrizi et al. 2009). This suggests that the particle size distributions of the aerosol can be tuned according to the intended application either by increasing the gas flow rate (above the minimum gas flow rate that ensures stable high frequency operation) or by adding a clean gas flow (dilution) downstream of the spark generator.

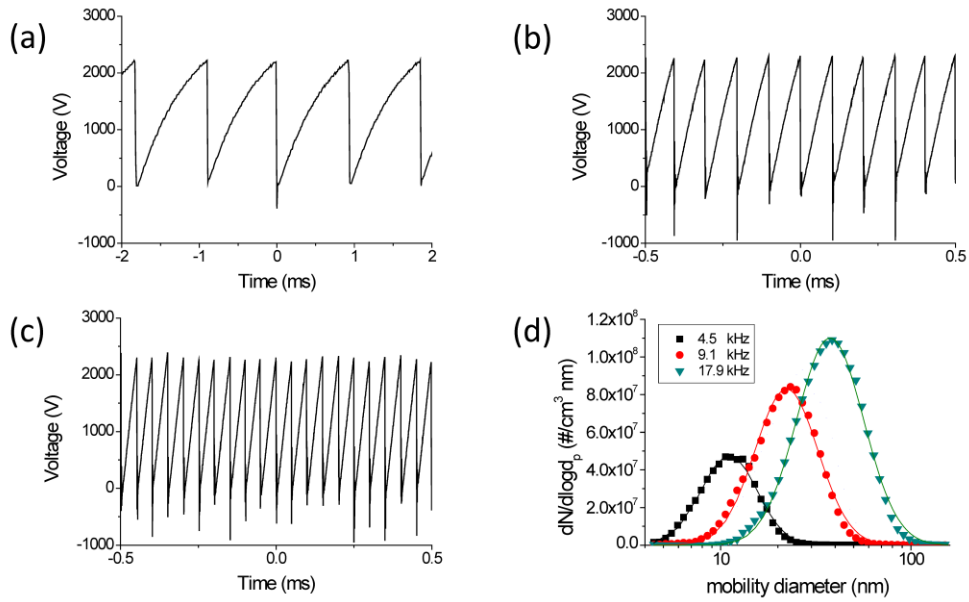

Figure 5.6. Voltage profiles from wire-to-plate electrode type spark discharger at different frequency: (a) 4.5 kHz, (b) 9.1 kHz and (c) 17.9 kHz. (d) Size distribution of generated nanoparticles at each frequency showing increasing geometric mean diameter and total number concentration as the frequency increases.

5.4. Conclusion

We have developed a high frequency spark discharge generator using wire-to-plate electrode configuration that enables fast removal of spark plasma and compared its performance to rod-to-rod and wire-to-rod electrode configurations to identify process parameters that determine the maximum stable spark frequency that can be achieved. By observing the current and voltage profiles of the spark discharge events, rapid plasma removal characterized by short spark duration was identified as an important feature of stable spark discharges at high frequencies for our wire-to-plate electrode spark discharger. High-intensity electric fields and fast carrier gas flows within the spark zone were both found to contribute to faster plasma removal, and therefore to stable high frequency operation. Among the three electrode configurations compared, wire-to-plate electrodes were best suited to implement both means, achieving spark stability up to 17.9 kHz. Using the wire-to-plate electrodes, it was shown that the mass production rate of nanoparticles indeed scale linearly with the spark frequency, as long as no premature spark discharges occur, in which case the mass production rate drops off sharply. Increasing the spark frequency leads to particle agglomerates of increasing mean diameter, and hence appropriate measures should be taken when designing large industrial-scale spark discharge generators for production of nanoparticles with a specific size distribution.

5.5. References

Borra, J.-P. (2006). Nucleation and aerosol processing in atmospheric pressure electrical discharges: powders production, coatings and filtration. Journal of Physics D: Applied Physics 39:R19.

Chae, S., Lee, D., Kim, M.-C., Kim, D. S., Choi, M. (2015). Wire-in-Hole-Type Spark Discharge Generator for Long-Time Consistent Generation of Unagglomerated Nanoparticles. Aerosol Science and Technology 49:463-471.

Ha, K., Jang, E., Jang, S., Lee, J.-K., Jang, M. S., Choi, H., Cho, J.-S., Choi, M. (2016). A light-trapping strategy for nanocrystalline silicon thin-film solar cells using three-dimensionally assembled nanoparticle structures. Nanotechnology 27:055403.

Han, K., Kim, W., Yu, J., Lee, J., Lee, H., Woo, C. G., Choi, M. (2012). A study of pin-to-plate type spark discharge generator for producing unagglomerated nanoaerosols. Journal of Aerosol Science 52:80-88.

Jang, S., Yoon, J., Ha, K., Kim, M.-C., Kim, D. H., Kim, S. M., Kang, S. M., Park, S. J., Jung, H. S., Choi, M. (2016). Facile fabrication of three-dimensional TiO 2 structures for highly efficient perovskite solar cells. Nano Energy 22:499-506.

Jung, K., Hahn, J., In, S., Bae, Y., Lee, H., Pikhitsa, P. V., Ahn, K., Ha, K., Lee, J. K., Park, N., Choi, M. (2014). Hotspot-Engineered 3D Multipetal Flower Assemblies for Surface-Enhanced Raman

Spectroscopy. Advanced Materials 26:5924-5929.

Kim, M.-C., Kim, B. J., Yoon, J., Lee, J.-W., Suh, D., Park, N.-G., Choi, M., Jung, H. S. (2015). Electro-spray deposition of a mesoporous TiO 2 charge collection layer: toward large scale and continuous production of high efficiency perovskite solar cells. Nanoscale 7:20725-20733.

Lee, H., You, S., Pikhitsa, P. V., Kim, J., Kwon, S., Woo, C. G., Choi, M. (2010). Three-dimensional assembly of nanoparticles from charged aerosols. Nano letters 11:119-124.

Maisser, A., Barmpounis, K., Attoui, M., Biskos, G., Schmidt-Ott, A. (2015). Atomic Cluster Generation with an Atmospheric Pressure Spark Discharge Generator. Aerosol Science and Technology 49:886-894.

Messing, M. E., Dick, K. A., Wallenberg, L. R., Deppert, K. (2009). Generation of size-selected gold nanoparticles by spark discharge—for growth of epitaxial nanowires. Gold Bulletin 42:20-26.

Meuller, B. O., Messing, M. E., Engberg, D. L., Jansson, A. M., Johansson, L. I., Norlén, S. M., Tureson, N., Deppert, K. (2012). Review of spark discharge generators for production of nanoparticle aerosols. Aerosol Science and Technology 46:1256-1270.

Park, K.-T., Farid, M. M., Hwang, J. (2014). Anti-agglomeration of spark discharge-generated aerosols via unipolar air ions. Journal of Aerosol Science 67:144-156.

Pfeiffer, T., Feng, J., Schmidt-Ott, A. (2014). New developments in spark

production of nanoparticles. Advanced Powder Technology 25:56-70.

Schwyn, S., Garwin, E., Schmidt-Ott, A. (1988). Aerosol generation by spark discharge. Journal of Aerosol Science 19:639-642.

Sung, H., Lee, J., Han, K., Lee, J.-K., Sung, J., Kim, D., Choi, M., Kim, C. (2014). Controlled positioning of metal nanoparticles in an organic light-emitting device for enhanced quantum efficiency. Organic Electronics 15:491-499.

Tabrizi, N. S., Ullmann, M., Vons, V., Lafont, U., Schmidt-Ott, A. (2009). Generation of nanoparticles by spark discharge. Journal of Nanoparticle Research 11:315-332.

Acknowledgement

This work was supported by the Global Frontier R&D Program on Center for Multiscale Energy System funded by the National Research Foundation (NRF) under the Ministry of Science, ICT and Future Planning, Korea (Grant no. 2011-0031561 and 2012M3A6A7054855).

국문 초록

스파크 방전법을 이용한 반도체 나노입자의 고효율 합성법

서울대학교 대학원 기계항공공학부

이 동 준

나노입자는 새로운 광학적 및 전기적 특성으로 인해 다양한 응용 분야에서 널리 연구되고 사용되고 있다. 그 중에서도 양자점(quantum dot)이라 불리는 결정성 반도체 나노입자는 크기에 따라 에너지 갭을 변화시키는 양자 구속 효과 (quantum confinement effect)라는 고유한 특성을 가지고 있어 태양전지, 레이저 및 LED와 같은 다양한 응용 분야에서 연구, 응용되고 있다. 이러한 양자점의 합성법은 나노 기술의 연구에 있어서 중요한 주제가 되어왔다. 지금까지, 결정성 반도체 나노입자는 일반적으로 액상 합성법을 사용하여 제조되었으며, 이는 유독한 전구체를 다뤄야 하는 문제점과 불순물 및 부산물과 같은 단점을 가지고 있다.

많은 에어로졸 기반 기상 합성법은 기존의 콜로이드 방법이 충족시키지 못하는 깨끗하고 효율적으로 기능성 나노입자를 생산하

는 방법으로 각광받아왔다. 그 중에서도, 최근에는 간단하고 효율적인 실험 방법으로 하전된 에어로졸을 제조할 수 있는 스파크 방전법이 주목받아왔으며, 스파크 방전을 통해 생성된 나노 입자는 10 nm 미만의 입자를 효율적으로 제조하는데 적합한 기술인 것으로 연구되어 왔다. 이를 바탕으로, 본 논문에서는 스파크 방전을 이용한 결정성 반도체 나노입자의 합성 방법을 개발하고 장기 안정성과 생산량을 향상시켜 입자 생성 효율을 향상시키고자 한다.

결정성 반도체 나노입자를 합성하기 위해, 환원성 기체인 수소 기체를 스파크 방전법에 도입하였다. 이송 기체로 수소 가스를 주입함으로써, 산화물 입자를 효과적으로 제거할 수 있는 환원 분위기가 생성되었고, 고에너지의 스파크 방전에 의해 해리된 수소 기체가 나노 입자에 침투하여 결정화 과정에 기여하였다. 결과적으로, 높은 순도와 결정성을 갖는, 수소원자로 표면 처리가 된 실리콘 나노입자를 수소를 이용한 스파크 방전법을 통해 성공적으로 합성하였다.

또한 Ⅳ족 반도체 이외에 Ⅲ-Ⅴ 족 반도체인 갈륨-비소 나노결정을 유사한 방법으로 합성하였다. 수소가 입자 내부로부터 빠져나오는 과정은 더욱 복잡하고 특정한 에너지가 필요하기 때문에 결정화 과정과 결함 회복을 위해 두 개의 열처리 공정이 추가적으로 수행되었다. 높은 결정성을 가지면서 갈륨 비소간 비율이 1:1인 갈륨비소 양자점이 합성되었고 가시광 영역에서 광발광(photoluminescence) 특성을 측정함으로써 양자 구속 효과를 확인할 수 있었다.

생성 된 나노입자의 실용적 이용을 위해, 입자 생성의 장기 안정성을 향상시키는 연구를 수행하였다. 새로 설계된 타입의 스파크 방전기는 봉-봉 구조 및 핀-판 구조인 기존의 스파크 방전기

와 비교하여 장시간에 걸쳐 일정한 크기 분포를 갖는 응집되지 않은 나노입자를 생성 할 수 있었다. 새롭게 설계된 스파크 방전기는 전극 형태 및 갭 거리의 변화를 효과적으로 억제하여 방전 전압 및 스파크 주파수의 변화를 최소화하는 것이 가능하였다.

마지막으로, 나노 입자의 대량 생산을 위해 고주파 영역에서 안정적인 스파크 방전 상태를 유지하기 위한 전선 대 전극 구조를 제시 하였다. 기존의 스파크 방전기에 비해 이 새로운 발전기는 전극의 비대칭 구조로 인해 훨씬 높은 전기장을 가지고, 입자 발생 구역에서 훨씬 빠른 유속으로 인해 스파크 방전 후의 잔류 플라즈마를 효과적으로 소멸시킬 수 있다. 새롭게 설계된 스파크 방전을 사용하여 최대 17.9 kHz 까지의 안정된 주파수를 달성할 수 있었고 나노입자의 생산량 역시 스파크 주파수에 비례하여 증가하였다.

주요어: 스파크 방전법; 양자점; 수소 도입 스파크 방전; 장기안정성; 고주파 스파크 방전

학 번: 2011-22892